Micromagnetic simulation of magnetofossils with realistic size and shape distributions: Linking magnetic proxies with nanoscale observations and implications for magnetofossil identification

Liao Chang[1,2*], Richard J. Harrison[3], Thomas A. Berndt[1]

* Correspondence to: liao.chang@pku.edu.cn (L. Chang)

1. Laboratory of Orogenic Belts and Crustal Evolution, School of Earth and Space Sciences, Peking University, Beijing 100871, P. R. China
2. Laboratory for Marine Geology, Qingdao National Laboratory for Marine Science and Technology, Qingdao 266071, P. R. China
3. Department of Earth Sciences, University of Cambridge, Cambridge CB2 3EQ, UK

Abstract We build micromagnetic models to investigate the magnetic properties of biogenic magnetite – a common type of magnetic minerals that is responsible for recording a wide range of biological, geophysical and geological processes on earth. The geometry of modelled particles is based on realistic size and shape distributions from nanoscale observations. Systematic changes in microstructures of biogenic magnetite ensembles are built and their magnetic properties are calculated, which enables a quantitative and separate assessment of the effect of crystal morphology and chain structures. Although the same particle size and shape distributions are used in all calculations, simulation results document large variations in magnetic properties, i.e., wide distributions of coercivity (B_c = ~10-60 mT), coercivity of remanence (B_{cr} = ~14-81 mT), dispersion parameter (DP = ~0.1-0.5), and skewness values (S = ~0.7-1.1) due to variable degree of anisotropy and magnetostatic interactions. Previously, the commonly observed “biogenic soft” and “biogenic hard” components on biogenic magnetite-bearing samples were often interpreted to reflect crystal

morphologies, and that the small DP values of coercivity distributions were an indication of narrow particle size distributions. Our simulations suggest that these speculations are not always the case and that magnetosome microstructures likely exert a dominant control over their magnetic properties. Our modelling results provide a new theoretical perspective on the magnetic properties of biogenic magnetite, which is important for understanding magnetic proxy signals from magnetofossils in a wide range of environmental and geological settings, and for the search for biogenic magnetite in terrestrial rocks and in extra-terrestrial materials.

1. Introduction

Magnetic nanoparticles synthesized intracellularly by magnetotactic bacteria (MTB) are a widely distributed source of magnetic materials in natural environments (Faivre and Schüler, 2008). MTB are a diverse group of aquatic prokaryotes that biomineralize membrane-enclosed magnetic nanoparticles (magnetosomes) of either magnetite (Fe_3O_4) or greigite (Fe_3S_4). Magnetosomes are typically arranged in chains which act as microscopic compasses, passively orienting the bacterial cells in the geomagnetic field in order to aid their search for the optimal living conditions. Biogenic magnetite crystals can be buried and preserved in sediments as magnetofossils that retain information about a wide range of biological, environmental, geophysical and geological processes. Recent studies indicate that magnetofossils are widely distributed in sediments and sedimentary rocks (e.g., Kopp and Kirschvink, 2008; Roberts et al., 2012, 2013). Magnetofossil records are widely used in earth sciences, including reconstructions of paleomagnetic field behaviour (e.g., Roberts et al., 2012), past marine productivity (e.g., Roberts et al., 2011; Yamazaki, 2012, Yamazaki and Ikehara, 2012), and other paleoenvironmental conditions (e.g., Kopp and Kirschvink, 2008; Chang et al., 2012, 2013, 2018; Usui et al., 2017).

Magnetofossil identification and robust interpretation of magnetofossil records require a thorough understanding of the natural variability of their magnetic properties. Several studies demonstrate the potential importance of magnetofossil morphologies in controlling magnetic properties. By analyzing a large set of lacustrine and marine sediments, Egli (2004) identified two distinct groups of biogenic magnetite: biogenic soft (BS) and biogenic hard (BH) components, which were suggested to correspond to different magnetofossil morphologies, i.e. BH and BS components are related to more elongated and more equant magnetite crystals, respectively. Such magnetic fingerprints are suggested for tracing environmental conditions (Egli, 2004). The presence of BS and BH signatures was widely reported and was used for various paleoenvironmental reconstructions (e.g., Yamazaki, 2012; Chang et al., 2013; Roberts et al., 2013; Heslop et al., 2014). The origin of BS and BH components in sedimentary records was tested by transmission electron microscopic (TEM) imaging, which indicated a casual link between magnetofossil morphologies and magnetic properties (e.g., Yamazaki and Ikehara, 2012; Lascu and Plank, 2013; Usui et al., 2017; Chang et al., 2018). However, the origin of BS and BH components remain elusive. The strong effect of magnetosome chain structures on rock magnetic properties is demonstrated by experimental observations (e.g., Kobayashi et al., 2006; Kopp et al., 2006; Li et al., 2012) and numerical simulations (e.g., Harrison and Lascu, 2014). The large variation in experimental coercivity values of samples containing different MTB strains and on magnetofossil-bearing sediments suggests that their magnetic properties are controlled either through crystal morphologies or chain architectures. But it has been difficult to isolate the two effects and analyse each quantitatively, because a numerical tool that directly links crystal morphologies, chain structures, and magnetic properties is not yet available. This limits significantly the use of magnetic proxies extracted from magnetofossil records.

In this study, we build three-dimensional micromagnetic models using realistic size and shape distributions to simulate magnetofossil magnetic properties. The new micromagnetic model is based on a numerical model and software FORCulator developed previously by Harrison and Lascu (2014), which considers synthetic coercivity distributions. The new model here enables construction of magnetofossil assemblages using morphological data obtained from electron microscopic observations, and hence allows direct comparisons of experimental magnetic properties with theoretical calculations of magnetofossil ensembles with various microstructures. Our calculations enable a separate assessment of the effect of magnetofossil morphologies and microstructures on their magnetic properties. Therefore, the new numerical model provides a method to test potential biogenic magnetite chain structures within samples. Results from our simulation were compared with available experimental data. Our modelling study represents an important step forward for understanding the origin of the variability of magnetofossil magnetic properties, and ultimately for the inversion of magnetic properties into mineral assemblages within natural samples.

2. Micromagnetic model

2.1. Geometry

The input geometry of magnetofossil ensembles in our micromagnetic models was constructed using realistic size and shape distributions determined from TEM observations on natural samples. Biogenic magnetite particles often have specific crystal morphologies with sharp crystal edges. Theses crystals also have a narrow size ranges, and mostly within the ideal single domain (SD) size range (e.g., Faivre and Schüler, 2008). These characteristics were used to distinguish possible magnetofossil particles from other forms under TEM analysis (e.g., Petersen et al., 1986; Stoltz et al., 1986; Thomas-Keprta et al., 2000; Buseck et al., 2001; Chang et al., 2012; Yamazaki, 2012). Results from a typical natural sample, refer as

99 'Magnetofossil 146', with a dominant magnetofossil magnetic mineralogy were used. This
100 sample is a pelagic sediment from South Atlantic Ocean Drilling Program (ODP) Hole 1263C
101 (section 14H2A, 146-147 cm interval) at the onset of the the Palaeocene-Eocene Thermal
102 Maximum event. Detailed sample information and its magnetic properties were presented in
103 Chang et al. (2018). TEM images that show presence of abundant magnetofossil crystals are
104 provided in Figure 1a and in the supplementary Figure S1. Hysteresis parameters for this
105 sample and another two samples ('Magnetofossil 130' and 'Magnetofossil 110' from the
106 same ODP core) are presented in Table 1.
107 The size and shape of magnetofossil crystals in the TEM images were measured (Fig. 1a).
108 Since standard bright-field TEM images are a projection of a 3D objects onto a 2D plane, we
109 made an assumption that the observed biogenic magnetite crystals have a square cross section
110 such that the total volume of a particle is v = length a × width b × width b (Fig. 1a). This
111 assumption is necessary and simplifies the input geometry. In order to get statistically
112 significant distributions of crystal morphologies, we analysed 887 magnetofossil grains for
113 sample 'Magnetofossil 146'. The obtained distributions of particle length (Fig. 1b) and axial
114 ratio ($q = a/b$; Fig. 1c) were used to construct various magnetofossil microstructures for
115 micromagnetic calculations.
116 A two-step procedure was used to construct magnetofossil microstructures: (1) Building
117 individual magnetofossil chains (Fig. 1d). Magnetofossil crystals with variable sizes and
118 shapes were selected randomly from the TEM morphology "database" (Fig. 1a-c; Fig. S2-S3),
119 which were then assembled into various chain configurations by controlling their spatial
120 arrangements (Fig. 1d). Three parameters were considered to construct chains: 1) number of
121 magnetofossil grains in a chain ($1 \leq n \leq 30$); 2) particle gap between adjacent magnetofossil
122 grains ($1 \leq d \leq 50$ nm); and 3) degree of chain bending ($0 \leq c \leq 1$). To make sure there is no
123 physical overlap between magnetofossil crystals, the distance r between two adjacent

magnetofossil grains is controlled as the sum of half particle length and particle gap *d* (Fig. 1d). To model different degrees of chain bending, we use the same constrained, self-avoiding random walk procedure described by Harrison and Lascu (2014). (2) Placing chains in a box region at random orientations (Fig. 1f). The size of the box region was set to be 5 μm × 5 μm × 5 μm for all simulations. For each simulation, 300 magnetofossil crystals selected randomly from the morphology "database" were constructed, i.e. 30 chains × 10 particles per chain, or 60 chains × 5 particles per chain. Chains are sufficiently separated so that magnetostatic interaction between different magnetofossil chains are negligible. The input geometry for all our micromagnetic calculations were created based on a modified version of FORCulator (Harrison and Lascu, 2014). A brief description of modifications to the original FORCulator package is presented in the supplementary texts and Figures S2-S5.

2.2. Anisotropy

The shape anisotropy for elongated magnetite is given by:

$$B_c = \Delta N \cdot M_s \quad (1)$$

where ΔN is the difference between the self-demagnetizing factors along the particle width and length and M_s is room-temperature saturation magnetization for magnetite (M_s = 480 kAm^{-1}; Dunlop and Özdemir, 1997). Cubic anisotropy was not considered in our simulations. This simplification is reasonable because shape anisotropy dominates the anisotropy even when a magnetite grain is slightly elongated, e.g., length/width ratio >1.05. Most biogenic magnetite crystals have values well above this threshold. Shape anisotropy of individual magnetofossil particles was calculated using the analytical formula in Butler and Banerjee (1975). For elongated parallelepipeds with a square cross section, ΔN is (in cgs units):

$$\Delta N = 2\pi - 6g(1,q) \quad (2)$$

where $g(1,q) = [F(1,0) - F(1,q)]/q$ and q is the axial ratio. The expression for $F(1,q)$ is

149 $$F(1,q) = 2(1-q^2)\sinh^{-1}\left[(1+q^2)^{-\frac{1}{2}}\right] + 2(q^2)\sinh^{-1}\left(\frac{1}{q}\right) + 2q\tan^{-1}\left[q(2+\right.$$

150 $$q212-\pi q-231-q22+q212+231-2q21+q212+23q3 \qquad (3)$$

151 The micro-coercivity values for a range of elongated magnetite crystals as a function of
152 elongation are calculated (Fig. 1e). Micro-coercivity increases monotonically with increasing
153 q, but saturates for infinitely long grains. The micro-coercivity for each magnetofossil crystal
154 was computed and then used in the following micromagnetic calculations.
155
156 **2.3. Micromagnetic calculation**
157 Micromagnetic calculations in this study are based on interacting ensembles of stable SD
158 particles, i.e. Stoner and Wohlfarth (1948) type particles with coherent rotation in an applied
159 field. Each particle is treated as a point dipole with a magnetic moment determined by its
160 volume and M_s, and a uniaxial anisotropy determined by its elongation q (Harrison and Lascu,
161 2014). Additional information about our micromagnetic simulations is provided in the
162 supplementary materials. Magnetic moment distributions within a single grain were not
163 considered, which is a good approximation for all but the largest magnetofossils. These large
164 grains may in reality show some level of vorticity or flowering that would slightly reduce the
165 coercivity. Thermal fluctuations were similarly not considered. The size of modelled particles
166 (Fig. 1a-c) is well above the theoretical SP/SD threshold sizes (i.e. 17 and 12 nm for non-
167 interacting and interacting equidimensional SD grains, respectively; Muxworthy and
168 Williams, 2009). Therefore, the effect of thermal fluctuations, which can reduce coercivity,
169 on the modelled hysteresis properties here is negligible.
170 Such a simplified micromagnetic approach is ideal for modelling biogenic magnetite
171 assemblages with dominant SD properties. Compared to full micromagnetic simulation
172 (Muxworthy and Williams, 2006), which models detailed domain structures and magnetic
173 properties of a single grain or a small number of grains, this simplified micromagnetic method

174 is computationally rapid, which makes it efficient to compute large number of magnetic
175 particles with distributions of microstructures and orientations, as is the case for
176 magnetofossil ensembles. The method is particularly suited to calculating first-order reversal
177 curve (FORC) diagrams, which require the equilibrium magnetization of the ensemble to be
178 calculated for thousands of different applied magnetic fields and applied field histories.
179 The total effective magnetic field acting on each particle is calculated as the sum of the
180 applied magnetic field, the dipole-dipole interaction field, and the uniaxial anisotropy field.
181 The magnetic configuration is relaxed iteratively by placing each magnetization vector closer
182 to the local effective field vector throughout the ensemble. FORCs were simulated using a
183 modified version of FORCulator (Harrison and Lascu, 2014), with modelling parameters: B_c
184 limit of 0.16 T, B_u limit of 0.06 T, step size of 0.0025, 100 FORCs, and 100 averaging steps.
185 Hysteresis parameters (B_c, B_{cr}, M_{rs}/M_s, B_{cr}/B_c), coercivity profiles, and isothermal remanent
186 magnetization (IRM) curves were extracted from modelled FORC diagrams. IRM curves
187 were fitted by a skewed logarithmic Gaussian distribution, which is defined by three
188 parameters: a peak B_c value, a dispersion parameter (DP), and a skewness value S, using the
189 MAX UnMix web application (Maxbauer et al., 2016).
190
191 **3. Modelling results**
192 Simulated magnetic properties are presented in the frame of systematic changes in chain
193 structures with different values of n, d, and c.
194
195 **3.1. Variable degree of chain bending *c***
196 Randomly packed, randomly oriented chains of magnetofossil ensembles with a
197 systematic change in c were simulated (Fig. 2). In each simulation, modelled chains contain
198 10 crystals with an inter-particle separation of d = 20 nm. For straight chains (c = 0),

199 processed FORC diagrams contain a central ridge component along the $B_u = 0$ axis and a
200 negative distribution in the lower left region (Fig. 2a), which are characteristics of non-
201 interacting uniaxial SD particle assemblages (Newell, 2005; Egli et al., 2010). When
202 introducing a degree of chain bending, i.e. $c = 0.4$, a strong FORC central ridge remains (Fig.
203 2b), but the peak of the central ridge shifts to lower coercivity values compared to the case of
204 straight chains (Fig. 2a; Table 2). In addition, FORC distributions develop a weak wing above
205 and below the central ridge, associated with contributions from collapsed magnetosomes, that
206 contribute to an overall vertical broadening (Fig. 2b). The centre of these wings lies on the
207 left side of the central ridge with a lower coercivity. The FORC diagram for further collapsed
208 chains ($c = 0.8$) retains a clear central ridge but with a significantly stronger wing (Fig. 2c).
209 The peak of the central ridge shifts to even lower coercivity values (Table 2). Such modelled
210 bimodal FORC distributions are similar to those from experiments on MTB samples
211 containing collapsed magnetosome chains (Chen et al., 2007; Li et al., 2012) and
212 micromagnetic simulations (Harrison and Lascu, 2014). The effect of chain bending on
213 magnetic properties is also demonstrated in FORC profiles along the $B_u = 0$ axis (Fig. 2d),
214 which show coercivity changes due to chain bending. A similar trend was observed for
215 modelled coercivity of remanence (Fig. 2e; Table 2).
216
217 **3.2.Variable number of particles in a chain *n***
218 FORC diagrams were simulated for different numbers of particles in chains ($1 \leq n \leq 30$;
219 Fig. 3a-c, f-h). A constant particle separation of 20 nm was used. The cases of straight chains
220 (Fig. 3a-e) and fully collapsed chains (Fig. 3f-j) were modelled. All simulated FORC
221 diagrams for straight chains ($c = 0$) with different number of particles in a chain contain a
222 major sharp central ridge component along $B_u = 0$ and negative distributions in the lower left
223 region (Fig. 3a-c). The peak of modelled profiles for coercivity and coercivity of remanence

increases with increasing n (Fig. 3a-d). This is expected as more particles assembled in a straight chain enhance shape anisotropy. Our calculations indicate that, similar as previous report (Muxworthy and Williams, 2006), coercivity increases rapidly with increasing n for $n \leq 5$ for straight chains. Beyond 5, the increase in peak coercivity becomes insensitive to n and B_c is close to a saturation value of ~36 mT.

For the case of fully collapsed chains, magnetostatic interactions increase with n (Fig. 3f-h). Changes in coercivity distributions are less sensitive to increasing n (Fig. 3f-j). For example, coercivity values for different n are clustered around 18-20 mT (Table 2). The main difference is that the high field tail becomes larger and the coercivity distribution broader for the case of long collapsed chains compared to shorter chains (Fig. 3g, h).

3.3. Variable particle separation in a chain *d*

Micromagnetic models for a variety of particle separations (d = 1, 5, 10, 20, 30, and 50 nm) were built. All these models have chains containing 10 particles. Cases of straight chains (c = 0; Fig. 4a-e) and fully collapsed chains (c = 1; Fig. 4f-j) were simulated. Simulated FORC diagrams indicate that magnetic properties are sensitive to changing d. For straight chains, all the diagrams show a major central ridge component (Fig. 4a-c). With increasing d, the peak coercivity of central ridge shifts to lower values (Fig. 4d). Also distributions of backfield curves rapidly shift to lower values with increasing d (Fig. 4e; Table 2). B_c values drops from 53 mT for d = 5 nm to 18 mT for d = 50 nm.

For fully collapsed chains, modelled FORC diagrams contain a bimodal feature with a central ridge component and strong wings with a large vertical spread (Fig. 4f-h). Similar as for straight chains, peak coercivity and coercivity of remanence shift to lower values with increasing d (Fig. 4i, j; Table 2).

3.4. Sorted particle arrangement in a chain

We build models with sorted particle arrangement in a chain, where the volume of magnetofossil crystals decreases from the centre toward the ends of the chain (Fig. 5a). This configuration arguably better mimics the arrangement of particles observed in magnetotactic bacteria, where immature magnetosomes with smaller volumes are typically found at the ends of chains. Two scenarios were modelled: for the case of sorted chains with $c = 0$, $n = 10$, $d =$ 20 nm, simulated hysteresis parameters are: $B_c = 42.7$ mT, $B_{cr} = 51.2$ mT, $M_{rs}/M_s = 0.496$, $B_{cr}/B_c = 1.198$. Compare to randomly arranged chains (Table 2; Fig. 2), B_c increases ~27%, B_{cr} increases ~16% (Fig. 5d, e). For sorted chains with $c = 1$, $n = 10$, $d = 20$ nm, modelled hysteresis parameters were found to be: $B_c = 13.1$ mT, $B_{cr} = 30.7$ mT, $M_{rs}/M_s = 0.280$, $B_{cr}/B_c =$ 2.342. Compared to randomly arranged chains, B_c decreases ~30%, B_{cr} decreases ~10% (Fig. 5d, e). Features of the modelled FORC diagrams (Fig. 5b, c), as well as trend (as a function of c, n, d) are similar to those of randomly arranged particles in a chain.

4. Discussions

4.1 Origin of BS and BH components in sediments

Different MTB species contain distinct magnetosome morphologies and chain structures (e.g., Faivre and Schüler, 2008). These variations are reflected by variable hysteresis parameters measured on magnetosome-bearing samples (Table 1). Our micromagnetic simulations of realistic chain structures indicate large variations in coercivity distribution of biogenic magnetite as a function of chain structures (c, n, and d), i.e. simulated B_c and B_{cr} values range from ~9-61 mT, and ~14-81 mT, respectively (Table 2), even though the same particle size distribution was used (Figures 2-4). Those modelled coercivity values cover the coercivity range reported for BS and BH components of magnetofossil-bearing sediments and whole-cell MTB samples. Our micromagnetic simulations, therefore, indicate a strong effect

of chain structures on magnetic properties, as has also been demonstrated experimentally (e.g., Kobayashi et al., 2006; Kopp et al. 2006; Li et al., 2012). Li et al. (2012) presented a detailed experimental study, where they broke up intact magnetosome chains and formed particle clumps. Subsequent hysteresis and FORC measurements indicate a progressive change in coercivity distributions and magnetostatic interactions. Our micromagnetic simulations indicate similar trends in changing coercivity and magnetostatic interactions as experimental data: coercivity decreases, accompanied by increasing magnetostatic interactions, with increasing chain breakup and particle clumps. Magnetofossil crystal morphologies may have a first-order control over magnetic properties. Our simulations demonstrate the potentially strong role of chain structures on controlling magnetic properties, which in some cases could act as the dominant control. We suggest that the BS component is most likely related to assemblages containing relatively isolated particle, while the BH component mostly corresponds to magnetofossil particles in chains with a minor contribution from elongated particles. Therefore, the BS and BH components does not necessarily reflect changes in magnetosome morphologies, but chain alteration and preservation are likely more important. This highlights the need for developing analytical tools to determine the unknown magnetofossil chain structures preserved in sediments for paleoenvironmental interpretations.

4.2 Modelled trends of coercivity distributions

Each simulated backfield IRM curve was fitted by a skewed logarithmic Gaussian distribution (Figure 6; Egli, 2004; Maxbauer et al., 2016). Most simulated IRM curves can be fitted well with one component, explaining most data variability (Fig. 6). Peak B_c, DP, and S values were extracted from fitting (Table 2). To visualize effects of chain structures on modelled magnetic properties, hysteresis parameters and fitted IRM parameters are presented

298 in Day plot (Day et al., 1977; Dunlop, 2002; Fig. 7a), DP vs. peak B_c plot (Fig. 7b), and S vs.
299 peak B_c plot (Fig. 7c). We observe systematic trends with changing chain structures:
300 (1) Increasing c results in a general decrease in peak B_c with hysteresis ratios move to the
301 lower right region in the Day plot, an increase in DP (i.e. from ~0.1 to 0.28), and left-skewed
302 distributions (Table 2; open blue triangles in Fig. 7).
303 (2) With increasing n, hysteresis ratios move along the $M_{rs}/M_s = 0.5$ line to the left, peak
304 B_c increases, DP decreases (from ~0.21 to 0.1), and a drop in skewness (i.e., S values increase
305 from ~0.71 to 0.94) for straight chains (Table 2; open squares in Fig. 7). For collapsed chains
306 ($c = 1$), with increasing n, hysteresis ratios move towards the lower right region in the Day
307 plot (open red circles in Fig. 7a). Larger DP values (~0.23-0.31) compared to straight chains
308 are observed, which generally increase with increasing n (Table 2; open red circles in Fig. 7b).
309 S values increase from 0.81 ($n = 3$) to 1.05 ($n = 30$), indicating changes from left-skewed, to
310 more symmetric, and to slightly right-skewed (Table 2; open red circles in Fig. 7c).
311 (3) Changes in hysteresis ratios, DP and S values are relatively insensitive to changing d
312 for straight chains (open yellow circles in Fig. 7), i.e. DP and S values are all in narrow ranges
313 (~0.10-0.12, and ~0.84-0.93, respectively), except for a large change in B_c. A large increase in
314 peak B_c, small increase in DP (from 0.25 to 0.38), small decrease in S (from ~0.93 to 0.79) are
315 observed for collapsed chains (open purple diamonds in Fig. 7).
316 These simulation data are fundamentally important for understanding the intrinsic
317 magnetic properties of biogenic magnetite. For example, small DP values (i.e. <0.25)
318 commonly observed on MTB and magnetofossil-bearing samples are thought to reflect
319 narrow particle size distributions of biogenic magnetite. Our modelling results suggest that
320 this is not the case, because modelled DP values for isolated particles are very large (~0.5)
321 and DP values drop rapidly (to <0.21) when grains form even only short chains (Table 2; Fig.
322 7b). DP values also increase significantly with increasing degree of chain bending (Fig. 7b).

Therefore, it is likely that chain structures, rather than magnetosome grain size distributions, have a dominant control over the broadness of coercivity. In addition, ideal logarithmic Gaussian distributions with $S = 1$ are often used to fit a biogenic IRM component. Our modelled large variation in S values for different chain configurations suggest that skewed coercivity distribution is probably also an intrinsic property for biogenic magnetite.

4.3 Implications for identification and quantification of magnetofossils

The most direct method to identify and quantify magnetofossils is by TEM observations (e.g., Petersen et al., 1986; Stoltz et al., 1986; Kopp and Kirschvink, 2008; Chang et al., 2012; Yamazaki, 2012). Several rock magnetic methods were proposed for rapidly screening natural samples for possible magnetofossil occurrence (see review by Kopp and Kirschvink, 2008). These methods include analysis of IRM curves (Moskowitz et al., 1988; Egli, 2004), low-temperature magnetism (Moskowitz et al., 1993; Chang et al., 2013, 2016), FORC diagrams (Egli et al., 2010; Heslop et al., 2014), and ferromagnetic resonance (Weiss et al., 2004; Kopp et al., 2006; Chang et al., 2014), which utilize one or more characteristics of magnetosomes, such as narrow particle size distribution, SD behaviour, and chain arrangements. Our new modelling approach, which combines direct TEM observations of crystal morphologies and simulation of magnetic properties, represents an advance in characterising magnetofossils. Our approach not only provides a new approach for a more robust identification of magnetofossils, but also provides a way to test possible chain configurations within natural samples. For example, experimental data (Chang et al., 2018) can be compared with simulations to infer possible chain structures (Fig. 8). This comparison indicates that some simulated results fit better to experimental data, although a unique solution is difficult to achieve. Such analysis also makes FORC inversion possible.

Our numerical method, therefore, provides a new tool for testing the presence of magnetofossils in terrestrial materials and meteorites. For example, a contradicting origin of ultra-fine-grained magnetite identified at the Paleocene-Eocene boundary at North Atlantic coastal sites was proposed: either detrital (Kent et al., 2003; Wang et al., 2013), biogenic (Lippert and Zachos, 2007; Kopp et al., 2007), or both. Possible presence of biogenic magnetite crystals within the Martian meteorites ALH84001, which has been used as possible trace of microbial activity on ancient mars (McKay et al., 1996; Thomas-Keprta et al., 2000), but has been highly controversial (e.g., Buseck et al., 2001). Magnetic properties of such materials using grain size distribution from TEM observations assuming possible isolated/chain structures ca be simulated. Comparing simulation results with experimental magnetic data, as has been performed in this study, should provide a strong test for potential presence of chain structures that can be used to search for past microbial activity.

5. Conclusions

Micromagnetic calculations on the same particle assemblage indicate that magnetic properties are very sensitive to magnetofossil chain structures, i.e. when changing chain bending, number of particles in a chain and particle separation in a chain. Modelling results indicate that the commonly observed BS and BH components from magnetofossil ensembles do not necessarily reflect magnetofossil morphologies, and that variations in magnetofossil chain architectures are likely to play a more important role in controlling the magnetic properties of magnetofossil ensembles. The commonly observed small DP values (i.e. < 0.25) probably do not originate from a narrow size distribution. Instead, chain structures likely act as a dominant control on the broadness of coercivity. The new micromagnetic simulation tool enables a direct link between rock magnetism and nanoscale observations of magnetic mineral grains, and represents a further step towards FORC inversion of magnetic mineral

372 microstructures within natural samples by comparing simulations with experimental data. Our
373 results are important for the use of magnetic proxy signals from magnetofossils for
374 paleoenvironmental reconstructions, and for the identification of biogenic magnetite in
375 terrestrial and extra-terrestrial materials.
376
377 **Acknowledgements** This study is supported by the National Natural Science Foundation of
378 China (grants 41574060, 41722402) to LC. RJH acknowledges funding from the European
379 Research Council under the European Union's Seventh Framework Programme (FP/2007–
380 2013)/ERC grant agreement 320750. We thank Joe Kirschvink for valuable suggestions,
381 Bruce Buffett for editorial handling, and Bruce Moskowitz for providing constructive
382 comments that significantly improved this paper.
383

Table 1 Hysteresis data for some samples containing biogenic magnetite

Samples	B_c (mT)	B_{cr} (mT)	M_{rs}/M_s	B_{cr}/B_c	References
M-1	26.8	27.6	0.53	1.02	Moskowitz et al. (1988)
MV1	-	-	0.49	1.10	Moskowitz et al. (1993)
MS1	-	-	0.44	1.10	Moskowitz et al. (1993)
Uncultured	26.7	40.0	0.47	1.50	Pan et al. (2005)
Uncultured	33.4	45.5	0.51	1.36	Pan et al. (2005)
Uncultured	41.0	50.2	0.49	1.22	Lin and Pan (2009)
Giant rod	54.5	61.0	0.59	1.12	Li et al. (2010)
AMB	30.5	37.4	0.50	1.23	Li et al. (2012)
MV-1	35.7	43.5	0.47	1.22	Jovane et al. (2012)
AMB-1	4.7	11.2	0.25	2.40	Li et al. (2009)
AMB-1	14.2	18.2	0.45	1.28	Li et al. (2009)
AMB-1	18.1	23.3	0.45	1.29	Li et al. (2009)
A1a altered	25.2	33.8	0.43	1.34	Li et al. (2012)
A1b altered	23.2	31.2	0.43	1.34	Li et al. (2012)
A1c altered	21.3	29.6	0.44	1.39	Li et al. (2012)
A2a altered	9.2	15.1	0.24	1.64	Li et al. (2012)
A2b altered	15.8	25.1	0.32	1.59	Li et al. (2012)
A2c altered	15.0	23.6	0.33	1.57	Li et al. (2012)
A3a altered	7.9	14.7	0.22	1.86	Li et al. (2012)
A3b altered	15.4	24.4	0.32	1.58	Li et al. (2012)
A3c altered	15.3	24.4	0.32	1.59	Li et al. (2012)
Magnetofossil 146	19.5	41.0	0.24	2.10	Chang et al. (2018)
Magnetofossil 130	18.8	42.7	0.22	2.27	Chang et al. (2018)
Magnetofossil 110	19.2	44.2	0.22	2.31	Chang et al. (2018)

384

Table 2 Simulated hysteresis parameters and fitted IRM parameters

Modelling parameters			Modelled hysteresis parameters				Fitted IRM parameters		
n*	d (nm)*	c*	B_c (mT)	B_{cr} (mT)	M_{rs}/M_s	B_{cr}/B_c	Peak B_c (mT)	DP	S
10	20	0.0	33.5	44.0	0.498	1.314	1.639	0.099	0.897
10	20	0.2	31.4	41.7	0.495	1.329	1.617	0.110	0.879
10	20	0.4	27.5	37.9	0.475	1.377	1.571	0.132	0.806
10	20	0.6	23.1	33.7	0.447	1.459	1.528	0.162	0.848
10	20	0.8	19.3	31.1	0.397	1.614	1.489	0.211	0.840
10	20	1.0	18.8	34.0	0.353	1.810	1.519	0.278	0.965
1#	20	0.0	8.6	14.3	0.498	1.661	0.802	0.546	1.165
2	20	0.0	12.9	26.6	0.499	2.061	1.389	0.207	0.705
3	20	0.0	25.0	38.3	0.499	1.537	1.564	0.138	0.714
5	20	0.0	29.5	41.8	0.506	1.419	1.612	0.117	0.812
10	20	0.0	33.5	44.0	0.498	1.314	1.639	0.099	0.897
20	20	0.0	35.4	45.4	0.491	1.281	1.651	0.095	0.923
30	20	0.0	36.2	45.8	0.493	1.264	1.659	0.100	0.938
3	20	1.0	17.8	28.7	0.436	1.612	1.440	0.230	0.808
5	20	1.0	18.2	30.9	0.386	1.698	1.482	0.235	0.907
10	20	1.0	18.8	34.0	0.353	1.810	1.519	0.278	0.965
20	20	1.0	19.5	37.2	0.336	1.908	1.568	0.301	1.093
30	20	1.0	19.8	37.4	0.327	1.891	1.567	0.313	1.048
10	1	0.0	61.4	81.5	0.497	1.329	1.902	0.122	0.927
10	5	0.0	53.3	69.6	0.506	1.306	1.833	0.107	0.903
10	10	0.0	44.2	58.8	0.507	1.329	1.759	0.109	0.840
10	20	0.0	33.5	44.0	0.498	1.314	1.639	0.099	0.897
10	30	0.0	26.3	34.8	0.507	1.324	1.535	0.117	0.872
10	50	0.0	18.2	24.5	0.499	1.346	1.394	0.156	1.032
10	1	1.0	30.0	54.3	0.321	1.808	1.702	0.253	0.934
10	5	1.0	26.8	46.7	0.328	1.739	1.643	0.239	0.907
10	10	1.0	22.8	41.7	0.330	1.830	1.587	0.262	0.882
10	20	1.0	18.8	34.0	0.353	1.810	1.519	0.278	0.965
10	30	1.0	15.9	28.3	0.378	1.782	1.407	0.330	0.845
10	50	1.0	12.8	22.5	0.407	1.760	1.281	0.381	0.792

* n is the number of particles in a chain
* d is the particle gap in a chain
* c is the degree of chain bending
# this case also represents randomly oriented particles without chains

References

Buseck, P.R., Dunin-Borkowski, R.E., Devouard, B., Frankel, R.B., McCartney, M.R., Midgley, P.A., Posfai, M., Weyland, M., 2001. Magnetite morphology and life on Mars. Proc. Natl. Acad. Sci. USA 98, 13490–13495.

Butler, R.F., Banerjee, S.K., 1975. Theoretical single-domain grain size range in magnetite and titanomagnetite. J. Geophys. Res. 80, 4049–4058.

Chang, L., Roberts, A.P., Williams, W., Fitz Gerald, J.D., Larrasoaña, J.C., Jovane, L., Muxworthy, A.R., 2012. Giant magnetofossils and hyperthermal events. Earth Planet. Sci. Lett. 351–352, 258–269.

Chang, L., Winklhofer, M., Roberts, A.P., Heslop, D., Florindo, F., Dekkers, M.J., Krijgsman, W., Kodama, K., Yamamoto Y., 2013. Low-temperature magnetic properties of pelagic carbonates: Oxidation of biogenic magnetite and identification of magnetosome chains. J. Geophys. Res. Solid Earth 118, 6049–6065, doi:10.1002/2013JB010381.

Chang, L., Roberts, A.P., Winklhofer, M., Heslop, D., Dekkers, M.J., Krijgsman, W., Fitz Gerald, J.D., Smith, P., 2014. Magnetic detection and characterization of biogenic magnetic minerals: A comparison of ferromagnetic resonance and first-order reversal curve diagrams. J. Geophys. Res. Solid Earth 119, 6136–6158, doi:10.1002/2014JB011213.

Chang, L., Heslop, D., Roberts, A.P., Rey, D., Mohamed, K.J., 2016. Discrimination of biogenic and detrital magnetite through a double Verwey transition temperature. J. Geophys. Res. Solid Earth 121, 3–14, doi:10.1002/ 2015JB012485.

Chang, L., Harrison, R.J. Zeng, F., Berndt, T.A., Roberts, A.P., Heslop, D., Zhao, X., 2018. Coupled microbial bloom and oxygenation decline recorded by magnetofossils during the Palaeocene-Eocene Thermal Maximum. Nat. Comm. 9, 4007, doi:10.1038/s41467-018-06472-y.

413 Chen, A.P., Egli, R., Moskowitz, B.M., 2007. First-order reversal curve (FORC) diagrams of natural
414 and cultured biogenic magnetic particles. J. Geophys. Res. 112, B08S90,
415 doi:10.1029/2006JB004575.
416 Day, R., Fuller, M., Schmidt, V.A., 1977. Hysteresis properties of titanomagnetites: Grain size and
417 composition dependence. Phys. Earth Planet. Inter. 13(4), 260–267, doi:10.1016/0031-
418 9201(77)90108-X.
419 Dunlop, D.J., 2002. Theory and application of the day plot (M_{rs}/M_s versus H_{cr}/H_c) 1. Theoretical
420 curves and tests using titanomagnetite data. J. Geophys. Res. 107(B3), 2056,
421 doi.org/10.1029/2001JB000486.
422 Dunlop, D.J., Özdemir Ö., 1997. Rock Magnetism: Fundamentals and Frontiers. Cambridge, 573 pp.
423 Egli, R., 2004. Characterization of individual rock magnetic components by analysis of remanence
424 curves, 1. Unmixing natural sediments. Stud. Geophys. Geod. 48, 391–446.
425 Egli, R., 2013. VARIFORC: an optimized protocol for calculating non-regular first-order reversal
426 curve (FORC) diagrams. Global Planet. Change 110, 302–320.
427 Egli, R., Chen, A.P., Winklhofer, M., Kodama, K.P., Horng, C.S., 2010. Detection of
428 noninteracting single domain particles using first-order reversal curve diagrams. Geochem.
429 Geophys. Geosyst. 11, doi:10.1029/2009GC002916.
430 Faivre, D., Schüler, D., 2008. Magnetotactic bacteria and magnetosomes. Chem. Rev. 108, 4875–
431 4898, doi:10.1021/cr078258w.
432 Harrison, R.J. Feinberg, J.M., 2008. FORCinel: an improved algorithm for calculating first-order
433 reversal curve distributions using locally weighted regression smoothing. Geochem. Geophys.
434 Geosyst. 9, doi:10.1029/2008GC001987.
435 Harrison, R.J., Lascu, I., 2014. FORCulator: a micromagnetic tool for simulating first-order
436 reversal curve diagrams. Geochem. Geophys. Geosyst. 15, 4671–4691.

437 Heslop, D., Roberts, A.P., Chang, L., 2014. Characterizing magnetofossils from first-order reversal
438 curve (FORC) central ridge signatures. Geochem. Geophys. Geosyst. 15, 2170–2179,
439 doi:10.1002/2014GC005291.
440 Jovane, L., Florindo, F., Bazylinski, D.A., Lins, U., 2012. Prismatic magnetite magnetosomes from
441 cultivated Magnetovibrio blakemorei strain MV-1: a magnetic fingerprint in marine
442 sediments? Environ. Microbial. Rep. 4(6), 664–668.
443 Kent, D.V., Cramer, B.S., Lanci, L., Wang, D., Wright, J.D., van der Voo, R., 2003. A case for a
444 comet impact trigger for the Paleocene/Eocene thermal maximum and carbon isotope
445 excursion. Earth Planet. Sci. Lett. 211, 13–26.
446 Kobayashi, A., Kirschvink, J.L., Nash, C.Z., Kopp, R.E., Sauer, D.A., Bertani, L.E., Voorhout, W.
447 F., Taguchi, T., 2006. Experimental observation of magnetosome chain collapse in
448 magnetotactic bacteria: sedimentological, paleomagnetic, and evolutionary implications. Earth
449 Planet. Sci. Lett. 245, 538–550.
450 Kopp, R.E., Kirschvink, J.L., 2008. The identification and biogeochemical interpretation of fossil
451 magnetotactic bacteria. Earth Sci. Rev. 86, 42–61.
452 Kopp, R.E., Weiss, B.P., Maloof, A.C., Vali, H., Nash, C.Z., Kirschvink, J.L., 2006. Chains,
453 clumps, and strings: Magnetofossil taphonomy with ferromagnetic resonance spectroscopy.
454 Earth Planet. Sci. Lett. 247, 10–25.
455 Kopp, R.E., Raub, T.D., Schumann, D., Vali, H., Smirnov, A.V., Kirschvink, J.L., 2007.
456 Magnetofossil spike during the Paleocene-Eocene thermal maximum: ferromagnetic resonance,
457 rock magnetic, and electron microscopy evidence from Ancora, New Jersey, United States.
458 Paleoceanography 22, PA4103, doi:10.1029/2007PA001473.
459 Lascu, I., Plank, C., 2013. A new dimension to sediment magnetism: Charting the spatial variability
460 of magnetic properties across lake basins. Global Planet. Change 110, 340–349.

461 Li, J.H., Pan, Y.X., Chen, G.J., Liu, Q.S., Tian, L.X., Lin, W., 2009. Magnetite magnetosome and
462 fragmental chain formation of Magnetospirillum magneticum AMB-1: Transmission electron
463 microscopy and magnetic observations. Geophys. J. Int. 177, 33–42, doi:10.1111/j.1365-
464 246X.2009.04043.x.
465 Li, J.H., Pan, Y.X., Liu, Q.S., Zhang, K.Y., Menguy, N., Che, R.C., Qin, H.F., Lin, W., Wu, W.F.,
466 Petersen, N., Yang, X., 2010. Biomineralization, crystallography and magnetic properties of
467 bullet-shaped magnetite magnetosomes in giant rod magnetotactic bacteria. Earth Planet. Sci.
468 Lett. 293, 368–376.
469 Li, J., Wu, W., Liu, Q., Pan, Y., 2012. Magnetic anisotropy, magnetostatic interactions and
470 identification of magnetofossils. Geochem. Geophys. Geosyst. 13, Q10Z51,
471 doi:10.1029/2012GC004384.
472 Lin, W., Pan, Y.X., 2009. Uncultivated magnetotactic cocci from Yuandadu Park in Beijing, China.
473 Appl. Environ. Microbiol. 75, 4046–4052, doi:10.1128/AEM.00247-09.
474 Lippert, P.C., Zachos, J.C., 2007. A biogenic origin for anomalous fine-grained magnetic material
475 at the Paleocene-Eocene boundary at Wilson Lake, New Jersey. Paleoceanography 22, PA4104,
476 doi:10.1029/ 2007PA001471.
477 Maxbauer, D.P., Feinberg, J.M., Fox, D.L., 2016. MAX UnMix: A web application for unmixing
478 magnetic coercivity distributions. Computers & Geosciences 95, 140–145.
479 McKay, D., Gibson, E., Thomas-Keprta, K., Vali, H., Romanek, C., Clemett, S., Chillier, X.,
480 Maechling, C., Zare, R., 1996. Search for past life on Mars: possible relic biogenic activity in
481 Martian meteorite ALH84001. Science 273, 924–930.
482 Moskowitz, B.M., Frankel, R.B., Flanders, P.J., Blakemore, R.P, Schwartz, B.B., 1988. Magnetic
483 properties of magnetotactic bacteria. J. Magn. Magn. Mater. 73, 273–288, doi:10.1016/0304-
484 8853(88)90093-5.

485 Moskowitz, B.M., Frankel, R.B., Bazylinski, D.A., 1993. Rock magnetic criteria for the detection
486 of biogenic magnetite. Earth Planet. Sci. Lett. 120, 283–300, doi:10.1016/0012-
487 821X(93)90245-5.
488 Muxworthy, A.R., Williams, W., 2006. Critical single-domain/multidomain grain sizes in
489 noninteracting and interacting elongated magnetite particles: Implications for magnetosomes. J.
490 Geophys. Res. 111(12), 1–7, doi:10.1029/2006JB004588.
491 Muxworthy, A.R., Williams, W., 2009. Critical superparamagnetic/single-domain grain sizes in
492 interacting magnetite particles: implications for magnetosome crystals. J. R. Soc. Interface 6,
493 1207–1212, doi:10.1098/rsif.2008.0462.
494 Newell, A.J., 2005. A high-precision model of first-order reversal curve (FORC) functions for
495 single-domain ferromagnets with uniaxial anisotropy. Geochem. Geophys. Geosyst. 6, Q05010,
496 doi:10.1029/2004GC000877.
497 Pan, Y., Petersen, N., Winklhofer, M., Davila, A.F., Liu, Q., Frederichs, T., Hanzlik, M., Zhu, R.,
498 2005. Rock magnetic properties of uncultured magnetotactic bacteria. Earth Planet. Sci. Lett.
499 237, 311–325, doi:10.1016/j.epsl.2005.06.029.
500 Petersen, N., von Dobeneck, T., Vali, H., 1986. Fossil bacterial magnetite in deep-sea sediments
501 from the South Atlantic Ocean. Nature 320, 611–614.
502 Roberts, A.P., Florindo, F., Villa, G., Chang, L., Jovane, L., Bohaty, S.M., Larrasoaña, J.C., Heslop,
503 D., Fitz Gerald, J.D., 2011. Magnetotactic bacterial abundance in pelagic marine environments
504 is limited by organic carbon flux and availability of dissolved iron. Earth Planet. Sci. Lett. 310,
505 441–452.
506 Roberts, A.P., Chang, L., Heslop, D., Florindo, F., Larrasoaña, J.C., 2012. Searching for single
507 domain magnetite in the ‘pseudo-single-domain’ sedimentary haystack: Implications of
508 biogenic magnetite preservation for sediment magnetism and relative paleointensity
509 determinations. J. Geophys. Res. 117, B08104, doi:10.1029/2012JB009412.

510 Roberts, A.P., Florindo, F., Chang, L., Heslop, D., Jovane, L., Larrasoanã, J.C., 2013. Magnetic
511 properties of pelagic marine carbonates. Earth Sci. Rev. 127, 111–139.
512 Stoltz, J.F., Chang, S.B.R., Kirschvink, J.L., 1986. Magnetotactic bacteria and single-domain
513 magnetite in hemipelagic sediments. Nature 321, 849–851.
514 Stoner, E.C., Wohlfarth, E.P., 1948. A mechanism of magnetic hysteresis in heterogeneous alloys.
515 Phil. Trans. R. Soc. London A240, 599–642.
516 Thomas-Keprta, K.L., Bazylinski, B.A., Kirchvink, J.L., Clemett, S.J., McKay, D.S., Wentworth,
517 S.J., Vali, H., Gibson, J.E.K., Romanek, C.S., 2000. Elongated prismatic magnetite crystals in
518 ALH84001 carbonate globules: potential Martian magnetofossils. Geochim. Cosmochim. Acta
519 64, 4049–4081.
520 Usui, Y., Yamazaki, T., Saitoh, M., 2017. Changing abundance of magnetofossil morphologies in
521 pelagic red clay around Minamitorishima, Western North Pacific. Geochem. Geophys. Geosyst.
522 18, 4558–4572, doi:10.1002/2017GC007127.
523 Wang, H, Kent, D.V., Jackson, M.J., 2013. Evidence for abundant isolated magnetic nanoparticles
524 at the Paleocene-Eocene boundary. Proc. Natl. Acad. Sci. USA 110, 425–430.
525 Weiss, B.P., Kim, S.S., Kirschvink, J.L., Kopp, R.E., Sankaran, M., Kobayashi, A., Komeili, A.,
526 2004. Ferromagnetic resonance and low temperature magnetic tests for biogenic magnetite.
527 Earth Planet. Sci. Lett. 224, 73–89.
528 Yamazaki, T., Ikehara, M., 2012. Origin of magnetic mineral concentration variation in the
529 Southern Ocean. Paleoceanography 27, PA2206.
530 Yamazaki, T., 2012. Paleoposition of Intertropical Convergence Zone in the eastern Pacific inferred
531 from glacial-interglacial changes in terrigenous and biogenic magnetic mineral fractions.
532 Geology 40, 151–154.
533

Figure captions

Figure 1 Procedures to build input models for micromagnetic calculations in this study. (a) An example of a bright-field TEM image, from which magnetofossil size and shape are determined. *a* and *b* define magnetofossil length and width, respectively. $1/q = b/a$ is the axial ratio. Arrows indicate magnetofossil crystals. (b, c) Histograms of the length and axial ratio of magnetofossil particles obtained by counting a large number of grains for sample 'magnetofossil 146'. This size and shape data were used for all following micromagnetic calculations. (d) Geometry of an individual chain generated by controlling a few parameters: particle gap *d* (typically 5-50 nm), chain bending *c* (0-1), and number of particles in a chain *n* (typically 2-30). In (d), 10 magnetofossil crystals in a chain were modelled (marked by numbers 1-10). Arrows indicate the direction of particle length, which also define the magnetic easy axis. Definition of grain volume, axial ratio and particle gap is shown. (e) Calculated micro-coercivity originated from shape anisotropy as a function of elongation *q* and axial ratio ($1/q$). The calculation is based on the analytical formula of (1-3). (f) An example of ensembles of magnetofossil chains generated with random chain orientations. Each chain contains 10 particles with a chain bending factor $c = 0.4$ and a particle gap $d = 20$ nm.

Figure 2 Micromagnetic simulations of the effect of chain bending *c*. (a-c) Examples of simulated FORC diagrams with variable *c*. (d) Extracted coercivity profiles along $B_u = 0$. (e) Extracted coercivity of remanence profiles. Different degree of chain bending was modelled ($c = 0$, 0.2, 0.4, 0.6, 0.8, 1.0), other modelling parameters were kept the same: $d = 20$ nm, $n = 10$. FORC diagrams were processed using FORCinel (Harrison and Feinberg, 2008) with VARIFORC smoothing parameters (Egli, 2013): $\{s_{c0}, s_{c1}, s_{b0}, s_{b1}, \lambda_c, \lambda_b\} = \{5, 5, 2, 5, 0.1, 0.1\}$ in (a, b), and $\{8, 8, 2, 8, 0.1, 0.1\}$ in (c).

Figure 3 Micromagnetic simulations of the effect of variable *n*: number of magnetofossil particles in a chain for (a-e) straight chains ($c = 0$), and (f-j) fully collapsed chains ($c = 1$). (a-c, f-h) Simulated FORC diagrams with variable *n*. (d, i) Extracted coercivity profiles along $B_u = 0$. (e, j) Extracted coercivity of remanence profiles. Variable number of particle in a chain was modelled ($n = 2, 3, 5, 10, 20, 30$), the same particle gap of 20 nm was used. VARIFORC smoothing parameters: $\{s_{c0}, s_{c1}, s_{b0}, s_{b1}, \lambda_c, \lambda_b\} = \{5, 5, 2, 5, 0.1, 0.1\}$ in (a-c, f), $\{10, 10, 2, 10, 0.1, 0.1\}$ in (g), and $\{12, 12, 2, 12, 0.1, 0.1\}$ in (h).

Figure 4 Micromagnetic simulations of the effect of variable *d*: particle separation in a chain for (a-e) straight chains ($c = 0$), and (f-j) fully collapsed chains ($c = 1$). (a-c, f-h) Simulated FORC diagrams with different magnetofossil particle separation in a chain. (d, i) Extracted coercivity profiles along $B_u = 0$. (e, j) Extracted coercivity of remanence profiles. Variable particle separations in a chain were modelled ($d = 1, 5, 10, 20, 30, 50$ nm), a constant $n = 10$ was used. VARIFORC smoothing parameters: $\{s_{c0}, s_{c1}, s_{b0}, s_{b1}, \lambda_c, \lambda_b\} = \{7, 7, 2, 7, 0.1, 0.1\}$ in (a-c), and $\{10, 10, 2, 10, 0.1, 0.1\}$ in (f-h).

Figure 5 Micromagnetic simulations of the effect of sorted particles in magnetofossil chains. (a) An example of ensembles of sorted particles in chains. This chain ensemble was built with $n = 10$, $c = 0.3$, and $d = 20$ nm. (b, c) Examples of simulated FORC diagrams. Comparison of sorted particles and random particles in chains for (d) coercivity profiles along $B_u = 0$, and (e) B_{cr} profiles. VARIFORC smoothing parameters: $\{s_{c0}, s_{c1}, s_{b0}, s_{b1}, \lambda_c, \lambda_b\} = \{5, 5, 2, 5, 0.1, 0.1\}$ in (b), and $\{10, 10, 2, 10, 0.1, 0.1\}$ in (c).

Figure 6 Examples of fitting of simulated IRM curves using Max UnMix (Maxubauer et al., 2016). Black lines with gray dots are IRM data from micromagnetic simulation. Red dashed lines are the best fit with a skewed logarithmic Gaussian distribution. Parameters, i.e. peak B_c, *DP* and *S* values from fitted components are indicated.

Figure 7 Plots of simulated hysteresis parameters and fitted IRM parameters from micromagnetic data. (a) Hysteresis ratios in a Day plot (Day et al., 1977). (b) Plot of *DP versus* Peak B_c. (c) Plot of *S versus* peak B_c. In (a), solid black circles are data of whole cell MTB samples (Moskowitz et al., 1988, 1993; Pan et al., 2005; Li et al., 2009, 2010, 2012; Lin and Pan, 2009), solid red circles are MTB samples containing immature magnetosome crystals and chains (Li et al., 2009), open circles are experimental data of MTB samples with altered magnetosome chains, i.e. collapsed and clumped chains (Li et al., 2012). Solid black lines in (a) are the theoretical mixing curves of Dunlop (2002) in a Day plot. In (b), solid black circles are data of a whole cell MTB strain MV-1 sample (Jovane et al., 2012). In (a-c), open blue squares are modelled data with different degree of chain bending ($0 \leq c \leq 1$, $n = 10$, $d = 20$ nm). Open green squares are data with different number of particles in a chain for straight chains ($2 \leq n \leq 30$, $c = 0$, $d = 20$ nm). Open red circles are data with different number of particles in a chain for fully collapsed chains ($2 \leq n \leq 30$, $c = 1$, $d = 20$ nm). Open yellow circles are data with different particle separations in a chain for straight chains ($1 \leq d \leq 50$ nm, $c = 0$, $n = 10$). Open purple diamonds are data with different particle separations in a chain for fully collapsed chains ($1 \leq d \leq 50$ nm, $c = 1$, $n = 10$). Arrows indicate data trend with increasing controlling parameters (c, n, d). Legends apply to all plots.

Figure 8 Comparison of experimental B_{cr} distributions (thick black line) and numerical simulations (color lines). The experimental data (Chang et al., 2018) are normalized to maximum value. All simulated data are scaled. Arrows indicate trend from D+EX (detrital plus extracellular magnetite), to BS and to BH (Egli, 2004). 'Isolated non-interacting' refers to assemblage containing particles picked randomly from the TEM database and were placed far away from each other so that there are no magnetostatic interactions among particles.

***Highlights (for review)**

- Micromagnetic model considering realistic magnetofossil morphology data were built
- Micromagnetic calculations document large variations in magnetic properties
- Microstructure is a more important control of magnetic properties than morphology
- The numerical method provides a powerful tool for tracing past microbial activities

Micromagnetic simulation of magnetofossils with realistic size and shape distributions: Linking magnetic proxies with nanoscale observations and implications for magnetofossil identification

Liao Chang[1,2*], Richard J. Harrison[3], Thomas A. Berndt[1]

* Correspondence to: liao.chang@pku.edu.cn (L. Chang)

1. Laboratory of Orogenic Belts and Crustal Evolution, School of Earth and Space Sciences, Peking University, Beijing 100871, P. R. China
2. Laboratory for Marine Geology, Qingdao National Laboratory for Marine Science and Technology, Qingdao 266071, P. R. China
3. Department of Earth Sciences, University of Cambridge, Cambridge CB2 3EQ, UK

Abstract We build micromagnetic models to investigate the magnetic properties of biogenic magnetite – a common type of magnetic minerals that is responsible for recording a wide range of biological, geophysical and geological processes on earth. The geometry of modelled particles is based on realistic size and shape distributions from nanoscale observations. Systematic changes in microstructures of biogenic magnetite ensembles are built and their magnetic properties are calculated, which enables a quantitative and separate assessment of the effect of crystal morphology and chain structures. Although the same particle size and shape distributions are used in all calculations, simulation results document large variations in magnetic properties, i.e., wide distributions of coercivity (B_c = ~10-60 mT), coercivity of remanence (B_{cr} = ~14-81 mT), dispersion parameter (DP = ~0.1-0.5), and skewness values (S = ~0.7-1.1) due to variable degree of anisotropy and magnetostatic interactions. Previously, the commonly observed "biogenic soft" and "biogenic hard" components on biogenic magnetite-bearing samples were often interpreted to reflect crystal

morphologies, and that the small DP values of coercivity distributions were an indication of narrow particle size distributions. Our simulations suggest that these speculations are not always the case and that magnetosome microstructures likely exert a dominant control over their magnetic properties. Our modelling results provide a new theoretical perspective on the magnetic properties of biogenic magnetite, which is important for understanding magnetic proxy signals from magnetofossils in a wide range of environmental and geological settings, and for the search for biogenic magnetite in terrestrial rocks and in extra-terrestrial materials.

1. Introduction

Magnetic nanoparticles synthesized intracellularly by magnetotactic bacteria (MTB) are a widely distributed source of magnetic materials in natural environments (Faivre and Schüler, 2008). MTB are a diverse group of aquatic prokaryotes that biomineralize membrane-enclosed magnetic nanoparticles (magnetosomes) of either magnetite (Fe_3O_4) or greigite (Fe_3S_4). Magnetosomes are typically arranged in chains which act as microscopic compasses, passively orienting the bacterial cells in the geomagnetic field in order to aid their search for the optimal living conditions. Biogenic magnetite crystals can be buried and preserved in sediments as magnetofossils that retain information about a wide range of biological, environmental, geophysical and geological processes. Recent studies indicate that magnetofossils are widely distributed in sediments and sedimentary rocks (e.g., Kopp and Kirschvink, 2008; Roberts et al., 2012, 2013). Magnetofossil records are widely used in earth sciences, including reconstructions of paleomagnetic field behaviour (e.g., Roberts et al., 2012), past marine productivity (e.g., Roberts et al., 2011; Yamazaki, 2012, Yamazaki and Ikehara, 2012), and other paleoenvironmental conditions (e.g., Kopp and Kirschvink, 2008; Chang et al., 2012, 2013, 2018; Usui et al., 2017).

Magnetofossil identification and robust interpretation of magnetofossil records require a thorough understanding of the natural variability of their magnetic properties. Several studies demonstrate the potential importance of magnetofossil morphologies in controlling magnetic properties. By analyzing a large set of lacustrine and marine sediments, Egli (2004) identified two distinct groups of biogenic magnetite: biogenic soft (BS) and biogenic hard (BH) components, which were suggested to correspond to different magnetofossil morphologies, i.e. BH and BS components are related to more elongated and more equant magnetite crystals, respectively. Such magnetic fingerprints are suggested for tracing environmental conditions (Egli, 2004). The presence of BS and BH signatures was widely reported and was used for various paleoenvironmental reconstructions (e.g., Yamazaki, 2012; Chang et al., 2013; Roberts et al., 2013; Heslop et al., 2014). The origin of BS and BH components in sedimentary records was tested by transmission electron microscopic (TEM) imaging, which indicated a casual link between magnetofossil morphologies and magnetic properties (e.g., Yamazaki and Ikehara, 2012; Lascu and Plank, 2013; Usui et al., 2017; Chang et al., 2018). However, the origin of BS and BH components remain elusive. The strong effect of magnetosome chain structures on rock magnetic properties is demonstrated by experimental observations (e.g., Kobayashi et al., 2006; Kopp et al., 2006; Li et al., 2012) and numerical simulations (e.g., Harrison and Lascu, 2014). The large variation in experimental coercivity values of samples containing different MTB strains and on magnetofossil-bearing sediments suggests that their magnetic properties are controlled either through crystal morphologies or chain architectures. But it has been difficult to isolate the two effects and analyse each quantitatively, because a numerical tool that directly links crystal morphologies, chain structures, and magnetic properties is not yet available. This limits significantly the use of magnetic proxies extracted from magnetofossil records.

In this study, we build three-dimensional micromagnetic models using realistic size and shape distributions to simulate magnetofossil magnetic properties. The new micromagnetic model is based on a numerical model and software FORCulator developed previously by Harrison and Lascu (2014), which considers synthetic coercivity distributions. The new model here enables construction of magnetofossil assemblages using morphological data obtained from electron microscopic observations, and hence allows direct comparisons of experimental magnetic properties with theoretical calculations of magnetofossil ensembles with various microstructures. Our calculations enable a separate assessment of the effect of magnetofossil morphologies and microstructures on their magnetic properties. Therefore, the new numerical model provides a method to test potential biogenic magnetite chain structures within samples. Results from our simulation were compared with available experimental data. Our modelling study represents an important step forward for understanding the origin of the variability of magnetofossil magnetic properties, and ultimately for the inversion of magnetic properties into mineral assemblages within natural samples.

2. Micromagnetic model

2.1. Geometry

The input geometry of magnetofossil ensembles in our micromagnetic models was constructed using realistic size and shape distributions determined from TEM observations on natural samples. Biogenic magnetite particles often have specific crystal morphologies with sharp crystal edges. Theses crystals also have a narrow size ranges, and mostly within the ideal single domain (SD) size range (e.g., Faivre and Schüler, 2008). These characteristics were used to distinguish possible magnetofossil particles from other forms under TEM analysis (e.g., Petersen et al., 1986; Stoltz et al., 1986; Thomas-Keprta et al., 2000; Buseck et al., 2001; Chang et al., 2012; Yamazaki, 2012). Results from a typical natural sample, refer as

99 'Magnetofossil 146', with a dominant magnetofossil magnetic mineralogy were used. This
100 sample is a pelagic sediment from South Atlantic Ocean Drilling Program (ODP) Hole 1263C
101 (section 14H2A, 146-147 cm interval) at the onset of the the Palaeocene-Eocene Thermal
102 Maximum event. Detailed sample information and its magnetic properties were presented in
103 Chang et al. (2018). TEM images that show presence of abundant magnetofossil crystals are
104 provided in Figure 1a and in the supplementary Figure S1. Hysteresis parameters for this
105 sample and another two samples ('Magnetofossil 130' and 'Magnetofossil 110' from the
106 same ODP core) are presented in Table 1.
107 The size and shape of magnetofossil crystals in the TEM images were measured (Fig. 1a).
108 Since standard bright-field TEM images are a projection of a 3D objects onto a 2D plane, we
109 made an assumption that the observed biogenic magnetite crystals have a square cross section
110 such that the total volume of a particle is v = length a × width b × width b (Fig. 1a). This
111 assumption is necessary and simplifies the input geometry. In order to get statistically
112 significant distributions of crystal morphologies, we analysed 887 magnetofossil grains for
113 sample 'Magnetofossil 146'. The obtained distributions of particle length (Fig. 1b) and axial
114 ratio ($q = a/b$; Fig. 1c) were used to construct various magnetofossil microstructures for
115 micromagnetic calculations.
116 A two-step procedure was used to construct magnetofossil microstructures: (1) Building
117 individual magnetofossil chains (Fig. 1d). Magnetofossil crystals with variable sizes and
118 shapes were selected randomly from the TEM morphology "database" (Fig. 1a-c; Fig. S2-S3),
119 which were then assembled into various chain configurations by controlling their spatial
120 arrangements (Fig. 1d). Three parameters were considered to construct chains: 1) number of
121 magnetofossil grains in a chain ($1 \leq n \leq 30$); 2) particle gap between adjacent magnetofossil
122 grains ($1 \leq d \leq 50$ nm); and 3) degree of chain bending ($0 \leq c \leq 1$). To make sure there is no
123 physical overlap between magnetofossil crystals, the distance r between two adjacent

magnetofossil grains is controlled as the sum of half particle length and particle gap *d* (Fig. 1d). To model different degrees of chain bending, we use the same constrained, self-avoiding random walk procedure described by Harrison and Lascu (2014). (2) Placing chains in a box region at random orientations (Fig. 1f). The size of the box region was set to be 5 μm × 5 μm × 5 μm for all simulations. For each simulation, 300 magnetofossil crystals selected randomly from the morphology "database" were constructed, i.e. 30 chains × 10 particles per chain, or 60 chains × 5 particles per chain. Chains are sufficiently separated so that magnetostatic interaction between different magnetofossil chains are negligible. The input geometry for all our micromagnetic calculations were created based on a modified version of FORCulator (Harrison and Lascu, 2014). A brief description of modifications to the original FORCulator package is presented in the supplementary texts and Figures S2-S5.

2.2. Anisotropy

The shape anisotropy for elongated magnetite is given by:

$$B_c = \Delta N \cdot M_s \quad (1)$$

where ΔN is the difference between the self-demagnetizing factors along the particle width and length and M_s is room-temperature saturation magnetization for magnetite (M_s = 480 kAm^{-1}; Dunlop and Özdemir, 1997). Cubic anisotropy was not considered in our simulations. This simplification is reasonable because shape anisotropy dominates the anisotropy even when a magnetite grain is slightly elongated, e.g., length/width ratio >1.05. Most biogenic magnetite crystals have values well above this threshold. Shape anisotropy of individual magnetofossil particles was calculated using the analytical formula in Butler and Banerjee (1975). For elongated parallelepipeds with a square cross section, ΔN is (in cgs units):

$$\Delta N = 2\pi - 6g(1,q) \quad (2)$$

where $g(1,q) = [F(1,0) - F(1,q)]/q$ and q is the axial ratio. The expression for $F(1,q)$ is

149 $$F(1,q) = 2(1-q^2)\sinh^{-1}\left[(1+q^2)^{-\frac{1}{2}}\right] + 2(q^2)\sinh^{-1}\left(\frac{1}{q}\right) + 2q\tan^{-1}\left[q(2+\right.$$

150 $$q212-\pi q-231-q22+q212+231-2q21+q212+23q3 \quad (3)$$

151 The micro-coercivity values for a range of elongated magnetite crystals as a function of
152 elongation are calculated (Fig. 1e). Micro-coercivity increases monotonically with increasing
153 q, but saturates for infinitely long grains. The micro-coercivity for each magnetofossil crystal
154 was computed and then used in the following micromagnetic calculations.
155
156 **2.3. Micromagnetic calculation**
157 Micromagnetic calculations in this study are based on interacting ensembles of stable SD
158 particles, i.e. Stoner and Wohlfarth (1948) type particles with coherent rotation in an applied
159 field. Each particle is treated as a point dipole with a magnetic moment determined by its
160 volume and M_s, and a uniaxial anisotropy determined by its elongation q (Harrison and Lascu,
161 2014). Additional information about our micromagnetic simulations is provided in the
162 supplementary materials. Magnetic moment distributions within a single grain were not
163 considered, which is a good approximation for all but the largest magnetofossils. These large
164 grains may in reality show some level of vorticity or flowering that would slightly reduce the
165 coercivity. Thermal fluctuations were similarly not considered. The size of modelled particles
166 (Fig. 1a-c) is well above the theoretical SP/SD threshold sizes (i.e. 17 and 12 nm for non-
167 interacting and interacting equidimensional SD grains, respectively; Muxworthy and
168 Williams, 2009). Therefore, the effect of thermal fluctuations, which can reduce coercivity,
169 on the modelled hysteresis properties here is negligible.
170 Such a simplified micromagnetic approach is ideal for modelling biogenic magnetite
171 assemblages with dominant SD properties. Compared to full micromagnetic simulation
172 (Muxworthy and Williams, 2006), which models detailed domain structures and magnetic
173 properties of a single grain or a small number of grains, this simplified micromagnetic method

174 is computationally rapid, which makes it efficient to compute large number of magnetic
175 particles with distributions of microstructures and orientations, as is the case for
176 magnetofossil ensembles. The method is particularly suited to calculating first-order reversal
177 curve (FORC) diagrams, which require the equilibrium magnetization of the ensemble to be
178 calculated for thousands of different applied magnetic fields and applied field histories.
179 The total effective magnetic field acting on each particle is calculated as the sum of the
180 applied magnetic field, the dipole-dipole interaction field, and the uniaxial anisotropy field.
181 The magnetic configuration is relaxed iteratively by placing each magnetization vector closer
182 to the local effective field vector throughout the ensemble. FORCs were simulated using a
183 modified version of FORCulator (Harrison and Lascu, 2014), with modelling parameters: B_c
184 limit of 0.16 T, B_u limit of 0.06 T, step size of 0.0025, 100 FORCs, and 100 averaging steps.
185 Hysteresis parameters (B_c, B_{cr}, M_{rs}/M_s, B_{cr}/B_c), coercivity profiles, and isothermal remanent
186 magnetization (IRM) curves were extracted from modelled FORC diagrams. IRM curves
187 were fitted by a skewed logarithmic Gaussian distribution, which is defined by three
188 parameters: a peak B_c value, a dispersion parameter (DP), and a skewness value S, using the
189 MAX UnMix web application (Maxbauer et al., 2016).
190
191 **3. Modelling results**
192 Simulated magnetic properties are presented in the frame of systematic changes in chain
193 structures with different values of n, d, and c.
194
195 **3.1. Variable degree of chain bending *c***
196 Randomly packed, randomly oriented chains of magnetofossil ensembles with a
197 systematic change in c were simulated (Fig. 2). In each simulation, modelled chains contain
198 10 crystals with an inter-particle separation of d = 20 nm. For straight chains (c = 0),

199 processed FORC diagrams contain a central ridge component along the $B_u = 0$ axis and a
200 negative distribution in the lower left region (Fig. 2a), which are characteristics of non-
201 interacting uniaxial SD particle assemblages (Newell, 2005; Egli et al., 2010). When
202 introducing a degree of chain bending, i.e. $c = 0.4$, a strong FORC central ridge remains (Fig.
203 2b), but the peak of the central ridge shifts to lower coercivity values compared to the case of
204 straight chains (Fig. 2a; Table 2). In addition, FORC distributions develop a weak wing above
205 and below the central ridge, associated with contributions from collapsed magnetosomes, that
206 contribute to an overall vertical broadening (Fig. 2b). The centre of these wings lies on the
207 left side of the central ridge with a lower coercivity. The FORC diagram for further collapsed
208 chains ($c = 0.8$) retains a clear central ridge but with a significantly stronger wing (Fig. 2c).
209 The peak of the central ridge shifts to even lower coercivity values (Table 2). Such modelled
210 bimodal FORC distributions are similar to those from experiments on MTB samples
211 containing collapsed magnetosome chains (Chen et al., 2007; Li et al., 2012) and
212 micromagnetic simulations (Harrison and Lascu, 2014). The effect of chain bending on
213 magnetic properties is also demonstrated in FORC profiles along the $B_u = 0$ axis (Fig. 2d),
214 which show coercivity changes due to chain bending. A similar trend was observed for
215 modelled coercivity of remanence (Fig. 2e; Table 2).
216
217 **3.2.Variable number of particles in a chain *n***
218 FORC diagrams were simulated for different numbers of particles in chains ($1 \leq n \leq 30$;
219 Fig. 3a-c, f-h). A constant particle separation of 20 nm was used. The cases of straight chains
220 (Fig. 3a-e) and fully collapsed chains (Fig. 3f-j) were modelled. All simulated FORC
221 diagrams for straight chains ($c = 0$) with different number of particles in a chain contain a
222 major sharp central ridge component along $B_u = 0$ and negative distributions in the lower left
223 region (Fig. 3a-c). The peak of modelled profiles for coercivity and coercivity of remanence

224 increases with increasing n (Fig. 3a-d). This is expected as more particles assembled in a
225 straight chain enhance shape anisotropy. Our calculations indicate that, similar as previous
226 report (Muxworthy and Williams, 2006), coercivity increases rapidly with increasing n for $n \leq$
227 5 for straight chains. Beyond 5, the increase in peak coercivity becomes insensitive to n and
228 B_c is close to a saturation value of ~36 mT.
229 For the case of fully collapsed chains, magnetostatic interactions increase with n (Fig. 3f-
230 h). Changes in coercivity distributions are less sensitive to increasing n (Fig. 3f-j). For
231 example, coercivity values for different n are clustered around 18-20 mT (Table 2). The main
232 difference is that the high field tail becomes larger and the coercivity distribution broader for
233 the case of long collapsed chains compared to shorter chains (Fig. 3g, h).
234
235 **3.3. Variable particle separation in a chain *d***
236 Micromagnetic models for a variety of particle separations (d = 1, 5, 10, 20, 30, and 50
237 nm) were built. All these models have chains containing 10 particles. Cases of straight chains
238 (c = 0; Fig. 4a-e) and fully collapsed chains (c = 1; Fig. 4f-j) were simulated. Simulated
239 FORC diagrams indicate that magnetic properties are sensitive to changing d. For straight
240 chains, all the diagrams show a major central ridge component (Fig. 4a-c). With increasing d,
241 the peak coercivity of central ridge shifts to lower values (Fig. 4d). Also distributions of
242 backfield curves rapidly shift to lower values with increasing d (Fig. 4e; Table 2). B_c values
243 drops from 53 mT for d = 5 nm to 18 mT for d = 50 nm.
244 For fully collapsed chains, modelled FORC diagrams contain a bimodal feature with a
245 central ridge component and strong wings with a large vertical spread (Fig. 4f-h). Similar as
246 for straight chains, peak coercivity and coercivity of remanence shift to lower values with
247 increasing d (Fig. 4i, j; Table 2).
248

3.4. Sorted particle arrangement in a chain

We build models with sorted particle arrangement in a chain, where the volume of magnetofossil crystals decreases from the centre toward the ends of the chain (Fig. 5a). This configuration arguably better mimics the arrangement of particles observed in magnetotactic bacteria, where immature magnetosomes with smaller volumes are typically found at the ends of chains. Two scenarios were modelled: for the case of sorted chains with $c = 0$, $n = 10$, $d =$ 20 nm, simulated hysteresis parameters are: $B_c = 42.7$ mT, $B_{cr} = 51.2$ mT, $M_{rs}/M_s = 0.496$, $B_{cr}/B_c = 1.198$. Compare to randomly arranged chains (Table 2; Fig. 2), B_c increases ~27%, B_{cr} increases ~16% (Fig. 5d, e). For sorted chains with $c = 1$, $n = 10$, $d = 20$ nm, modelled hysteresis parameters were found to be: $B_c = 13.1$ mT, $B_{cr} = 30.7$ mT, $M_{rs}/M_s = 0.280$, $B_{cr}/B_c =$ 2.342. Compared to randomly arranged chains, B_c decreases ~30%, B_{cr} decreases ~10% (Fig. 5d, e). Features of the modelled FORC diagrams (Fig. 5b, c), as well as trend (as a function of c, n, d) are similar to those of randomly arranged particles in a chain.

4. Discussions

4.1 Origin of BS and BH components in sediments

Different MTB species contain distinct magnetosome morphologies and chain structures (e.g., Faivre and Schüler, 2008). These variations are reflected by variable hysteresis parameters measured on magnetosome-bearing samples (Table 1). Our micromagnetic simulations of realistic chain structures indicate large variations in coercivity distribution of biogenic magnetite as a function of chain structures (c, n, and d), i.e. simulated B_c and B_{cr} values range from ~9-61 mT, and ~14-81 mT, respectively (Table 2), even though the same particle size distribution was used (Figures 2-4). Those modelled coercivity values cover the coercivity range reported for BS and BH components of magnetofossil-bearing sediments and whole-cell MTB samples. Our micromagnetic simulations, therefore, indicate a strong effect

of chain structures on magnetic properties, as has also been demonstrated experimentally (e.g., Kobayashi et al., 2006; Kopp et al. 2006; Li et al., 2012). Li et al. (2012) presented a detailed experimental study, where they broke up intact magnetosome chains and formed particle clumps. Subsequent hysteresis and FORC measurements indicate a progressive change in coercivity distributions and magnetostatic interactions. Our micromagnetic simulations indicate similar trends in changing coercivity and magnetostatic interactions as experimental data: coercivity decreases, accompanied by increasing magnetostatic interactions, with increasing chain breakup and particle clumps. Magnetofossil crystal morphologies may have a first-order control over magnetic properties. Our simulations demonstrate the potentially strong role of chain structures on controlling magnetic properties, which in some cases could act as the dominant control. We suggest that the BS component is most likely related to assemblages containing relatively isolated particle, while the BH component mostly corresponds to magnetofossil particles in chains with a minor contribution from elongated particles. Therefore, the BS and BH components does not necessarily reflect changes in magnetosome morphologies, but chain alteration and preservation are likely more important. This highlights the need for developing analytical tools to determine the unknown magnetofossil chain structures preserved in sediments for paleoenvironmental interpretations.

4.2 Modelled trends of coercivity distributions

Each simulated backfield IRM curve was fitted by a skewed logarithmic Gaussian distribution (Figure 6; Egli, 2004; Maxbauer et al., 2016). Most simulated IRM curves can be fitted well with one component, explaining most data variability (Fig. 6). Peak B_c, DP, and S values were extracted from fitting (Table 2). To visualize effects of chain structures on modelled magnetic properties, hysteresis parameters and fitted IRM parameters are presented

298 in Day plot (Day et al., 1977; Dunlop, 2002; Fig. 7a), DP vs. peak B_c plot (Fig. 7b), and S vs.
299 peak B_c plot (Fig. 7c). We observe systematic trends with changing chain structures:
300 (1) Increasing c results in a general decrease in peak B_c with hysteresis ratios move to the
301 lower right region in the Day plot, an increase in DP (i.e. from ~0.1 to 0.28), and left-skewed
302 distributions (Table 2; open blue triangles in Fig. 7).
303 (2) With increasing n, hysteresis ratios move along the $M_{rs}/M_s = 0.5$ line to the left, peak
304 B_c increases, DP decreases (from ~0.21 to 0.1), and a drop in skewness (i.e., S values increase
305 from ~0.71 to 0.94) for straight chains (Table 2; open squares in Fig. 7). For collapsed chains
306 ($c = 1$), with increasing n, hysteresis ratios move towards the lower right region in the Day
307 plot (open red circles in Fig. 7a). Larger DP values (~0.23-0.31) compared to straight chains
308 are observed, which generally increase with increasing n (Table 2; open red circles in Fig. 7b).
309 S values increase from 0.81 ($n = 3$) to 1.05 ($n = 30$), indicating changes from left-skewed, to
310 more symmetric, and to slightly right-skewed (Table 2; open red circles in Fig. 7c).
311 (3) Changes in hysteresis ratios, DP and S values are relatively insensitive to changing d
312 for straight chains (open yellow circles in Fig. 7), i.e. DP and S values are all in narrow ranges
313 (~0.10-0.12, and ~0.84-0.93, respectively), except for a large change in B_c. A large increase in
314 peak B_c, small increase in DP (from 0.25 to 0.38), small decrease in S (from ~0.93 to 0.79) are
315 observed for collapsed chains (open purple diamonds in Fig. 7).
316 These simulation data are fundamentally important for understanding the intrinsic
317 magnetic properties of biogenic magnetite. For example, small DP values (i.e. <0.25)
318 commonly observed on MTB and magnetofossil-bearing samples are thought to reflect
319 narrow particle size distributions of biogenic magnetite. Our modelling results suggest that
320 this is not the case, because modelled DP values for isolated particles are very large (~0.5)
321 and DP values drop rapidly (to <0.21) when grains form even only short chains (Table 2; Fig.
322 7b). DP values also increase significantly with increasing degree of chain bending (Fig. 7b).

Therefore, it is likely that chain structures, rather than magnetosome grain size distributions, have a dominant control over the broadness of coercivity. In addition, ideal logarithmic Gaussian distributions with $S = 1$ are often used to fit a biogenic IRM component. Our modelled large variation in S values for different chain configurations suggest that skewed coercivity distribution is probably also an intrinsic property for biogenic magnetite.

4.3 Implications for identification and quantification of magnetofossils

The most direct method to identify and quantify magnetofossils is by TEM observations (e.g., Petersen et al., 1986; Stoltz et al., 1986; Kopp and Kirschvink, 2008; Chang et al., 2012; Yamazaki, 2012). Several rock magnetic methods were proposed for rapidly screening natural samples for possible magnetofossil occurrence (see review by Kopp and Kirschvink, 2008). These methods include analysis of IRM curves (Moskowitz et al., 1988; Egli, 2004), low-temperature magnetism (Moskowitz et al., 1993; Chang et al., 2013, 2016), FORC diagrams (Egli et al., 2010; Heslop et al., 2014), and ferromagnetic resonance (Weiss et al., 2004; Kopp et al., 2006; Chang et al., 2014), which utilize one or more characteristics of magnetosomes, such as narrow particle size distribution, SD behaviour, and chain arrangements. Our new modelling approach, which combines direct TEM observations of crystal morphologies and simulation of magnetic properties, represents an advance in characterising magnetofossils. Our approach not only provides a new approach for a more robust identification of magnetofossils, but also provides a way to test possible chain configurations within natural samples. For example, experimental data (Chang et al., 2018) can be compared with simulations to infer possible chain structures (Fig. 8). This comparison indicates that some simulated results fit better to experimental data, although a unique solution is difficult to achieve. Such analysis also makes FORC inversion possible.

Our numerical method, therefore, provides a new tool for testing the presence of magnetofossils in terrestrial materials and meteorites. For example, a contradicting origin of ultra-fine-grained magnetite identified at the Paleocene-Eocene boundary at North Atlantic coastal sites was proposed: either detrital (Kent et al., 2003; Wang et al., 2013), biogenic (Lippert and Zachos, 2007; Kopp et al., 2007), or both. Possible presence of biogenic magnetite crystals within the Martian meteorites ALH84001, which has been used as possible trace of microbial activity on ancient mars (McKay et al., 1996; Thomas-Keprta et al., 2000), but has been highly controversial (e.g., Buseck et al., 2001). Magnetic properties of such materials using grain size distribution from TEM observations assuming possible isolated/chain structures ca be simulated. Comparing simulation results with experimental magnetic data, as has been performed in this study, should provide a strong test for potential presence of chain structures that can be used to search for past microbial activity.

5. Conclusions

Micromagnetic calculations on the same particle assemblage indicate that magnetic properties are very sensitive to magnetofossil chain structures, i.e. when changing chain bending, number of particles in a chain and particle separation in a chain. Modelling results indicate that the commonly observed BS and BH components from magnetofossil ensembles do not necessarily reflect magnetofossil morphologies, and that variations in magnetofossil chain architectures are likely to play a more important role in controlling the magnetic properties of magnetofossil ensembles. The commonly observed small DP values (i.e. < 0.25) probably do not originate from a narrow size distribution. Instead, chain structures likely act as a dominant control on the broadness of coercivity. The new micromagnetic simulation tool enables a direct link between rock magnetism and nanoscale observations of magnetic mineral grains, and represents a further step towards FORC inversion of magnetic mineral

372 microstructures within natural samples by comparing simulations with experimental data. Our
373 results are important for the use of magnetic proxy signals from magnetofossils for
374 paleoenvironmental reconstructions, and for the identification of biogenic magnetite in
375 terrestrial and extra-terrestrial materials.
376
377 **Acknowledgements** This study is supported by the National Natural Science Foundation of
378 China (grants 41574060, 41722402) to LC. RJH acknowledges funding from the European
379 Research Council under the European Union's Seventh Framework Programme (FP/2007–
380 2013)/ERC grant agreement 320750. We thank Joe Kirschvink for valuable suggestions,
381 Bruce Buffett for editorial handling, and Bruce Moskowitz for providing constructive
382 comments that significantly improved this paper.
383

Table 1 Hysteresis data for some samples containing biogenic magnetite

Samples	B_c (mT)	B_{cr} (mT)	M_{rs}/M_s	B_{cr}/B_c	References
M-1	26.8	27.6	0.53	1.02	Moskowitz et al. (1988)
MV1	-	-	0.49	1.10	Moskowitz et al. (1993)
MS1	-	-	0.44	1.10	Moskowitz et al. (1993)
Uncultured	26.7	40.0	0.47	1.50	Pan et al. (2005)
Uncultured	33.4	45.5	0.51	1.36	Pan et al. (2005)
Uncultured	41.0	50.2	0.49	1.22	Lin and Pan (2009)
Giant rod	54.5	61.0	0.59	1.12	Li et al. (2010)
AMB	30.5	37.4	0.50	1.23	Li et al. (2012)
MV-1	35.7	43.5	0.47	1.22	Jovane et al. (2012)
AMB-1	4.7	11.2	0.25	2.40	Li et al. (2009)
AMB-1	14.2	18.2	0.45	1.28	Li et al. (2009)
AMB-1	18.1	23.3	0.45	1.29	Li et al. (2009)
A1a altered	25.2	33.8	0.43	1.34	Li et al. (2012)
A1b altered	23.2	31.2	0.43	1.34	Li et al. (2012)
A1c altered	21.3	29.6	0.44	1.39	Li et al. (2012)
A2a altered	9.2	15.1	0.24	1.64	Li et al. (2012)
A2b altered	15.8	25.1	0.32	1.59	Li et al. (2012)
A2c altered	15.0	23.6	0.33	1.57	Li et al. (2012)
A3a altered	7.9	14.7	0.22	1.86	Li et al. (2012)
A3b altered	15.4	24.4	0.32	1.58	Li et al. (2012)
A3c altered	15.3	24.4	0.32	1.59	Li et al. (2012)
Magnetofossil 146	19.5	41.0	0.24	2.10	Chang et al. (2018)
Magnetofossil 130	18.8	42.7	0.22	2.27	Chang et al. (2018)
Magnetofossil 110	19.2	44.2	0.22	2.31	Chang et al. (2018)

384

Table 2 Simulated hysteresis parameters and fitted IRM parameters

Modelling parameters			Modelled hysteresis parameters				Fitted IRM parameters		
n*	d (nm)*	c*	B_c (mT)	B_{cr} (mT)	M_{rs}/M_s	B_{cr}/B_c	Peak B_c (mT)	DP	S
10	20	0.0	33.5	44.0	0.498	1.314	1.639	0.099	0.897
10	20	0.2	31.4	41.7	0.495	1.329	1.617	0.110	0.879
10	20	0.4	27.5	37.9	0.475	1.377	1.571	0.132	0.806
10	20	0.6	23.1	33.7	0.447	1.459	1.528	0.162	0.848
10	20	0.8	19.3	31.1	0.397	1.614	1.489	0.211	0.840
10	20	1.0	18.8	34.0	0.353	1.810	1.519	0.278	0.965
1#	20	0.0	8.6	14.3	0.498	1.661	0.802	0.546	1.165
2	20	0.0	12.9	26.6	0.499	2.061	1.389	0.207	0.705
3	20	0.0	25.0	38.3	0.499	1.537	1.564	0.138	0.714
5	20	0.0	29.5	41.8	0.506	1.419	1.612	0.117	0.812
10	20	0.0	33.5	44.0	0.498	1.314	1.639	0.099	0.897
20	20	0.0	35.4	45.4	0.491	1.281	1.651	0.095	0.923
30	20	0.0	36.2	45.8	0.493	1.264	1.659	0.100	0.938
3	20	1.0	17.8	28.7	0.436	1.612	1.440	0.230	0.808
5	20	1.0	18.2	30.9	0.386	1.698	1.482	0.235	0.907
10	20	1.0	18.8	34.0	0.353	1.810	1.519	0.278	0.965
20	20	1.0	19.5	37.2	0.336	1.908	1.568	0.301	1.093
30	20	1.0	19.8	37.4	0.327	1.891	1.567	0.313	1.048
10	1	0.0	61.4	81.5	0.497	1.329	1.902	0.122	0.927
10	5	0.0	53.3	69.6	0.506	1.306	1.833	0.107	0.903
10	10	0.0	44.2	58.8	0.507	1.329	1.759	0.109	0.840
10	20	0.0	33.5	44.0	0.498	1.314	1.639	0.099	0.897
10	30	0.0	26.3	34.8	0.507	1.324	1.535	0.117	0.872
10	50	0.0	18.2	24.5	0.499	1.346	1.394	0.156	1.032
10	1	1.0	30.0	54.3	0.321	1.808	1.702	0.253	0.934
10	5	1.0	26.8	46.7	0.328	1.739	1.643	0.239	0.907
10	10	1.0	22.8	41.7	0.330	1.830	1.587	0.262	0.882
10	20	1.0	18.8	34.0	0.353	1.810	1.519	0.278	0.965
10	30	1.0	15.9	28.3	0.378	1.782	1.407	0.330	0.845
10	50	1.0	12.8	22.5	0.407	1.760	1.281	0.381	0.792

* n is the number of particles in a chain
* d is the particle gap in a chain
* c is the degree of chain bending
# this case also represents randomly oriented particles without chains

References

Buseck, P.R., Dunin-Borkowski, R.E., Devouard, B., Frankel, R.B., McCartney, M.R., Midgley, P.A., Posfai, M., Weyland, M., 2001. Magnetite morphology and life on Mars. Proc. Natl. Acad. Sci. USA 98, 13490–13495.

Butler, R.F., Banerjee, S.K., 1975. Theoretical single-domain grain size range in magnetite and titanomagnetite. J. Geophys. Res. 80, 4049–4058.

Chang, L., Roberts, A.P., Williams, W., Fitz Gerald, J.D., Larrasoaña, J.C., Jovane, L., Muxworthy, A.R., 2012. Giant magnetofossils and hyperthermal events. Earth Planet. Sci. Lett. 351–352, 258–269.

Chang, L., Winklhofer, M., Roberts, A.P., Heslop, D., Florindo, F., Dekkers, M.J., Krijgsman, W., Kodama, K., Yamamoto Y., 2013. Low-temperature magnetic properties of pelagic carbonates: Oxidation of biogenic magnetite and identification of magnetosome chains. J. Geophys. Res. Solid Earth 118, 6049–6065, doi:10.1002/2013JB010381.

Chang, L., Roberts, A.P., Winklhofer, M., Heslop, D., Dekkers, M.J., Krijgsman, W., Fitz Gerald, J.D., Smith, P., 2014. Magnetic detection and characterization of biogenic magnetic minerals: A comparison of ferromagnetic resonance and first-order reversal curve diagrams. J. Geophys. Res. Solid Earth 119, 6136–6158, doi:10.1002/2014JB011213.

Chang, L., Heslop, D., Roberts, A.P., Rey, D., Mohamed, K.J., 2016. Discrimination of biogenic and detrital magnetite through a double Verwey transition temperature. J. Geophys. Res. Solid Earth 121, 3–14, doi:10.1002/ 2015JB012485.

Chang, L., Harrison, R.J. Zeng, F., Berndt, T.A., Roberts, A.P., Heslop, D., Zhao, X., 2018. Coupled microbial bloom and oxygenation decline recorded by magnetofossils during the Palaeocene-Eocene Thermal Maximum. Nat. Comm. 9, 4007, doi:10.1038/s41467-018-06472-y.

413 Chen, A.P., Egli, R., Moskowitz, B.M., 2007. First-order reversal curve (FORC) diagrams of natural
414 and cultured biogenic magnetic particles. J. Geophys. Res. 112, B08S90,
415 doi:10.1029/2006JB004575.
416 Day, R., Fuller, M., Schmidt, V.A., 1977. Hysteresis properties of titanomagnetites: Grain size and
417 composition dependence. Phys. Earth Planet. Inter. 13(4), 260–267, doi:10.1016/0031-
418 9201(77)90108-X.
419 Dunlop, D.J., 2002. Theory and application of the day plot (M_{rs}/M_s versus H_{cr}/H_c) 1. Theoretical
420 curves and tests using titanomagnetite data. J. Geophys. Res. 107(B3), 2056,
421 doi.org/10.1029/2001JB000486.
422 Dunlop, D.J., Özdemir Ö., 1997. Rock Magnetism: Fundamentals and Frontiers. Cambridge, 573 pp.
423 Egli, R., 2004. Characterization of individual rock magnetic components by analysis of remanence
424 curves, 1. Unmixing natural sediments. Stud. Geophys. Geod. 48, 391–446.
425 Egli, R., 2013. VARIFORC: an optimized protocol for calculating non-regular first-order reversal
426 curve (FORC) diagrams. Global Planet. Change 110, 302–320.
427 Egli, R., Chen, A.P., Winklhofer, M., Kodama, K.P., Horng, C.S., 2010. Detection of
428 noninteracting single domain particles using first-order reversal curve diagrams. Geochem.
429 Geophys. Geosyst. 11, doi:10.1029/2009GC002916.
430 Faivre, D., Schüler, D., 2008. Magnetotactic bacteria and magnetosomes. Chem. Rev. 108, 4875–
431 4898, doi:10.1021/cr078258w.
432 Harrison, R.J. Feinberg, J.M., 2008. FORCinel: an improved algorithm for calculating first-order
433 reversal curve distributions using locally weighted regression smoothing. Geochem. Geophys.
434 Geosyst. 9, doi:10.1029/2008GC001987.
435 Harrison, R.J., Lascu, I., 2014. FORCulator: a micromagnetic tool for simulating first-order
436 reversal curve diagrams. Geochem. Geophys. Geosyst. 15, 4671–4691.

437 Heslop, D., Roberts, A.P., Chang, L., 2014. Characterizing magnetofossils from first-order reversal
438 curve (FORC) central ridge signatures. Geochem. Geophys. Geosyst. 15, 2170–2179,
439 doi:10.1002/2014GC005291.
440 Jovane, L., Florindo, F., Bazylinski, D.A., Lins, U., 2012. Prismatic magnetite magnetosomes from
441 cultivated Magnetovibrio blakemorei strain MV-1: a magnetic fingerprint in marine
442 sediments? Environ. Microbial. Rep. 4(6), 664–668.
443 Kent, D.V., Cramer, B.S., Lanci, L., Wang, D., Wright, J.D., van der Voo, R., 2003. A case for a
444 comet impact trigger for the Paleocene/Eocene thermal maximum and carbon isotope
445 excursion. Earth Planet. Sci. Lett. 211, 13–26.
446 Kobayashi, A., Kirschvink, J.L., Nash, C.Z., Kopp, R.E., Sauer, D.A., Bertani, L.E., Voorhout, W.
447 F., Taguchi, T., 2006. Experimental observation of magnetosome chain collapse in
448 magnetotactic bacteria: sedimentological, paleomagnetic, and evolutionary implications. Earth
449 Planet. Sci. Lett. 245, 538–550.
450 Kopp, R.E., Kirschvink, J.L., 2008. The identification and biogeochemical interpretation of fossil
451 magnetotactic bacteria. Earth Sci. Rev. 86, 42–61.
452 Kopp, R.E., Weiss, B.P., Maloof, A.C., Vali, H., Nash, C.Z., Kirschvink, J.L., 2006. Chains,
453 clumps, and strings: Magnetofossil taphonomy with ferromagnetic resonance spectroscopy.
454 Earth Planet. Sci. Lett. 247, 10–25.
455 Kopp, R.E., Raub, T.D., Schumann, D., Vali, H., Smirnov, A.V., Kirschvink, J.L., 2007.
456 Magnetofossil spike during the Paleocene-Eocene thermal maximum: ferromagnetic resonance,
457 rock magnetic, and electron microscopy evidence from Ancora, New Jersey, United States.
458 Paleoceanography 22, PA4103, doi:10.1029/2007PA001473.
459 Lascu, I., Plank, C., 2013. A new dimension to sediment magnetism: Charting the spatial variability
460 of magnetic properties across lake basins. Global Planet. Change 110, 340–349.

461 Li, J.H., Pan, Y.X., Chen, G.J., Liu, Q.S., Tian, L.X., Lin, W., 2009. Magnetite magnetosome and
462 fragmental chain formation of Magnetospirillum magneticum AMB-1: Transmission electron
463 microscopy and magnetic observations. Geophys. J. Int. 177, 33–42, doi:10.1111/j.1365-
464 246X.2009.04043.x.
465 Li, J.H., Pan, Y.X., Liu, Q.S., Zhang, K.Y., Menguy, N., Che, R.C., Qin, H.F., Lin, W., Wu, W.F.,
466 Petersen, N., Yang, X., 2010. Biomineralization, crystallography and magnetic properties of
467 bullet-shaped magnetite magnetosomes in giant rod magnetotactic bacteria. Earth Planet. Sci.
468 Lett. 293, 368–376.
469 Li, J., Wu, W., Liu, Q., Pan, Y., 2012. Magnetic anisotropy, magnetostatic interactions and
470 identification of magnetofossils. Geochem. Geophys. Geosyst. 13, Q10Z51,
471 doi:10.1029/2012GC004384.
472 Lin, W., Pan, Y.X., 2009. Uncultivated magnetotactic cocci from Yuandadu Park in Beijing, China.
473 Appl. Environ. Microbiol. 75, 4046–4052, doi:10.1128/AEM.00247-09.
474 Lippert, P.C., Zachos, J.C., 2007. A biogenic origin for anomalous fine-grained magnetic material
475 at the Paleocene-Eocene boundary at Wilson Lake, New Jersey. Paleoceanography 22, PA4104,
476 doi:10.1029/ 2007PA001471.
477 Maxbauer, D.P., Feinberg, J.M., Fox, D.L., 2016. MAX UnMix: A web application for unmixing
478 magnetic coercivity distributions. Computers & Geosciences 95, 140–145.
479 McKay, D., Gibson, E., Thomas-Keprta, K., Vali, H., Romanek, C., Clemett, S., Chillier, X.,
480 Maechling, C., Zare, R., 1996. Search for past life on Mars: possible relic biogenic activity in
481 Martian meteorite ALH84001. Science 273, 924–930.
482 Moskowitz, B.M., Frankel, R.B., Flanders, P.J., Blakemore, R.P, Schwartz, B.B., 1988. Magnetic
483 properties of magnetotactic bacteria. J. Magn. Magn. Mater. 73, 273–288, doi:10.1016/0304-
484 8853(88)90093-5.

485 Moskowitz, B.M., Frankel, R.B., Bazylinski, D.A., 1993. Rock magnetic criteria for the detection
486 of biogenic magnetite. Earth Planet. Sci. Lett. 120, 283–300, doi:10.1016/0012-
487 821X(93)90245-5.
488 Muxworthy, A.R., Williams, W., 2006. Critical single-domain/multidomain grain sizes in
489 noninteracting and interacting elongated magnetite particles: Implications for magnetosomes. J.
490 Geophys. Res. 111(12), 1–7, doi:10.1029/2006JB004588.
491 Muxworthy, A.R., Williams, W., 2009. Critical superparamagnetic/single-domain grain sizes in
492 interacting magnetite particles: implications for magnetosome crystals. J. R. Soc. Interface 6,
493 1207–1212, doi:10.1098/rsif.2008.0462.
494 Newell, A.J., 2005. A high-precision model of first-order reversal curve (FORC) functions for
495 single-domain ferromagnets with uniaxial anisotropy. Geochem. Geophys. Geosyst. 6, Q05010,
496 doi:10.1029/2004GC000877.
497 Pan, Y., Petersen, N., Winklhofer, M., Davila, A.F., Liu, Q., Frederichs, T., Hanzlik, M., Zhu, R.,
498 2005. Rock magnetic properties of uncultured magnetotactic bacteria. Earth Planet. Sci. Lett.
499 237, 311–325, doi:10.1016/j.epsl.2005.06.029.
500 Petersen, N., von Dobeneck, T., Vali, H., 1986. Fossil bacterial magnetite in deep-sea sediments
501 from the South Atlantic Ocean. Nature 320, 611–614.
502 Roberts, A.P., Florindo, F., Villa, G., Chang, L., Jovane, L., Bohaty, S.M., Larrasoaña, J.C., Heslop,
503 D., Fitz Gerald, J.D., 2011. Magnetotactic bacterial abundance in pelagic marine environments
504 is limited by organic carbon flux and availability of dissolved iron. Earth Planet. Sci. Lett. 310,
505 441–452.
506 Roberts, A.P., Chang, L., Heslop, D., Florindo, F., Larrasoaña, J.C., 2012. Searching for single
507 domain magnetite in the ‘pseudo-single-domain’ sedimentary haystack: Implications of
508 biogenic magnetite preservation for sediment magnetism and relative paleointensity
509 determinations. J. Geophys. Res. 117, B08104, doi:10.1029/2012JB009412.

510 Roberts, A.P., Florindo, F., Chang, L., Heslop, D., Jovane, L., Larrasoanã, J.C., 2013. Magnetic
511 properties of pelagic marine carbonates. Earth Sci. Rev. 127, 111–139.
512 Stoltz, J.F., Chang, S.B.R., Kirschvink, J.L., 1986. Magnetotactic bacteria and single-domain
513 magnetite in hemipelagic sediments. Nature 321, 849–851.
514 Stoner, E.C., Wohlfarth, E.P., 1948. A mechanism of magnetic hysteresis in heterogeneous alloys.
515 Phil. Trans. R. Soc. London A240, 599–642.
516 Thomas-Keprta, K.L., Bazylinski, B.A., Kirchvink, J.L., Clemett, S.J., McKay, D.S., Wentworth,
517 S.J., Vali, H., Gibson, J.E.K., Romanek, C.S., 2000. Elongated prismatic magnetite crystals in
518 ALH84001 carbonate globules: potential Martian magnetofossils. Geochim. Cosmochim. Acta
519 64, 4049–4081.
520 Usui, Y., Yamazaki, T., Saitoh, M., 2017. Changing abundance of magnetofossil morphologies in
521 pelagic red clay around Minamitorishima, Western North Pacific. Geochem. Geophys. Geosyst.
522 18, 4558–4572, doi:10.1002/2017GC007127.
523 Wang, H, Kent, D.V., Jackson, M.J., 2013. Evidence for abundant isolated magnetic nanoparticles
524 at the Paleocene-Eocene boundary. Proc. Natl. Acad. Sci. USA 110, 425–430.
525 Weiss, B.P., Kim, S.S., Kirschvink, J.L., Kopp, R.E., Sankaran, M., Kobayashi, A., Komeili, A.,
526 2004. Ferromagnetic resonance and low temperature magnetic tests for biogenic magnetite.
527 Earth Planet. Sci. Lett. 224, 73–89.
528 Yamazaki, T., Ikehara, M., 2012. Origin of magnetic mineral concentration variation in the
529 Southern Ocean. Paleoceanography 27, PA2206.
530 Yamazaki, T., 2012. Paleoposition of Intertropical Convergence Zone in the eastern Pacific inferred
531 from glacial-interglacial changes in terrigenous and biogenic magnetic mineral fractions.
532 Geology 40, 151–154.
533

534 **Figure captions**

535 **Figure 1** Procedures to build input models for micromagnetic calculations in this study.
536 (a) An example of a bright-field TEM image, from which magnetofossil size and shape
537 are determined. *a* and *b* define magnetofossil length and width, respectively. $1/q = b/a$ is
538 the axial ratio. Arrows indicate magnetofossil crystals. (b, c) Histograms of the length
539 and axial ratio of magnetofossil particles obtained by counting a large number of grains
540 for sample 'magnetofossil 146'. This size and shape data were used for all following
541 micromagnetic calculations. (d) Geometry of an individual chain generated by
542 controlling a few parameters: particle gap *d* (typically 5-50 nm), chain bending *c* (0-1),
543 and number of particles in a chain *n* (typically 2-30). In (d), 10 magnetofossil crystals in
544 a chain were modelled (marked by numbers 1-10). Arrows indicate the direction of
545 particle length, which also define the magnetic easy axis. Definition of grain volume,
546 axial ratio and particle gap is shown. (e) Calculated micro-coercivity originated from
547 shape anisotropy as a function of elongation *q* and axial ratio ($1/q$). The calculation is
548 based on the analytical formula of (1-3). (f) An example of ensembles of magnetofossil
549 chains generated with random chain orientations. Each chain contains 10 particles with
550 a chain bending factor $c = 0.4$ and a particle gap $d = 20$ nm.

551 **Figure 2** Micromagnetic simulations of the effect of chain bending *c*. (a-c) Examples of
552 simulated FORC diagrams with variable *c*. (d) Extracted coercivity profiles along $B_u = 0$.
553 (e) Extracted coercivity of remanence profiles. Different degree of chain bending was
554 modelled ($c = 0$, 0.2, 0.4, 0.6, 0.8, 1.0), other modelling parameters were kept the same:
555 $d = 20$ nm, $n = 10$. FORC diagrams were processed using FORCinel (Harrison and
556 Feinberg, 2008) with VARIFORC smoothing parameters (Egli, 2013): $\{s_{c0}, s_{c1}, s_{b0}, s_{b1},$
557 $\lambda_c, \lambda_b\} = \{5, 5, 2, 5, 0.1, 0.1\}$ in (a, b), and $\{8, 8, 2, 8, 0.1, 0.1\}$ in (c).

Figure 3 Micromagnetic simulations of the effect of variable *n*: number of magnetofossil particles in a chain for (a-e) straight chains ($c = 0$), and (f-j) fully collapsed chains ($c = 1$). (a-c, f-h) Simulated FORC diagrams with variable *n*. (d, i) Extracted coercivity profiles along $B_u = 0$. (e, j) Extracted coercivity of remanence profiles. Variable number of particle in a chain was modelled ($n = 2, 3, 5, 10, 20, 30$), the same particle gap of 20 nm was used. VARIFORC smoothing parameters: $\{s_{c0}, s_{c1}, s_{b0}, s_{b1}, \lambda_c, \lambda_b\} = \{5, 5, 2, 5, 0.1, 0.1\}$ in (a-c, f), $\{10, 10, 2, 10, 0.1, 0.1\}$ in (g), and $\{12, 12, 2, 12, 0.1, 0.1\}$ in (h).

Figure 4 Micromagnetic simulations of the effect of variable *d*: particle separation in a chain for (a-e) straight chains ($c = 0$), and (f-j) fully collapsed chains ($c = 1$). (a-c, f-h) Simulated FORC diagrams with different magnetofossil particle separation in a chain. (d, i) Extracted coercivity profiles along $B_u = 0$. (e, j) Extracted coercivity of remanence profiles. Variable particle separations in a chain were modelled ($d = 1, 5, 10, 20, 30, 50$ nm), a constant $n = 10$ was used. VARIFORC smoothing parameters: $\{s_{c0}, s_{c1}, s_{b0}, s_{b1}, \lambda_c, \lambda_b\} = \{7, 7, 2, 7, 0.1, 0.1\}$ in (a-c), and $\{10, 10, 2, 10, 0.1, 0.1\}$ in (f-h).

Figure 5 Micromagnetic simulations of the effect of sorted particles in magnetofossil chains. (a) An example of ensembles of sorted particles in chains. This chain ensemble was built with $n = 10$, $c = 0.3$, and $d = 20$ nm. (b, c) Examples of simulated FORC diagrams. Comparison of sorted particles and random particles in chains for (d) coercivity profiles along $B_u = 0$, and (e) B_{cr} profiles. VARIFORC smoothing parameters: $\{s_{c0}, s_{c1}, s_{b0}, s_{b1}, \lambda_c, \lambda_b\} = \{5, 5, 2, 5, 0.1, 0.1\}$ in (b), and $\{10, 10, 2, 10, 0.1, 0.1\}$ in (c).

Figure 6 Examples of fitting of simulated IRM curves using Max UnMix (Maxubauer et al., 2016). Black lines with gray dots are IRM data from micromagnetic simulation. Red dashed lines are the best fit with a skewed logarithmic Gaussian distribution. Parameters, i.e. peak B_c, *DP* and *S* values from fitted components are indicated.

583 **Figure 7** Plots of simulated hysteresis parameters and fitted IRM parameters from
584 micromagnetic data. (a) Hysteresis ratios in a Day plot (Day et al., 1977). (b) Plot of *DP*
585 *versus* Peak B_c. (c) Plot of *S versus* peak B_c. In (a), solid black circles are data of whole
586 cell MTB samples (Moskowitz et al., 1988, 1993; Pan et al., 2005; Li et al., 2009, 2010,
587 2012; Lin and Pan, 2009), solid red circles are MTB samples containing immature
588 magnetosome crystals and chains (Li et al., 2009), open circles are experimental data of
589 MTB samples with altered magnetosome chains, i.e. collapsed and clumped chains (Li
590 et al., 2012). Solid black lines in (a) are the theoretical mixing curves of Dunlop (2002)
591 in a Day plot. In (b), solid black circles are data of a whole cell MTB strain MV-1
592 sample (Jovane et al., 2012). In (a-c), open blue squares are modelled data with
593 different degree of chain bending ($0 \leq c \leq 1$, $n = 10$, $d = 20$ nm). Open green squares are
594 data with different number of particles in a chain for straight chains ($2 \leq n \leq 30$, $c = 0$, d
595 $= 20$ nm). Open red circles are data with different number of particles in a chain for
596 fully collapsed chains ($2 \leq n \leq 30$, $c = 1$, $d = 20$ nm). Open yellow circles are data with
597 different particle separations in a chain for straight chains ($1 \leq d \leq 50$ nm, $c = 0$, $n = 10$).
598 Open purple diamonds are data with different particle separations in a chain for fully
599 collapsed chains ($1 \leq d \leq 50$ nm, $c = 1$, $n = 10$). Arrows indicate data trend with
600 increasing controlling parameters (c, n, d). Legends apply to all plots.
601 **Figure 8** Comparison of experimental B_{cr} distributions (thick black line) and numerical
602 simulations (color lines). The experimental data (Chang et al., 2018) are normalized to
603 maximum value. All simulated data are scaled. Arrows indicate trend from D+EX
604 (detrital plus extracellular magnetite), to BS and to BH (Egli, 2004). 'Isolated non-
605 interacting' refers to assemblage containing particles picked randomly from the TEM
606 database and were placed far away from each other so that there are no magnetostatic
607 interactions among particles.

Figure 1

Click here to download high resolution image

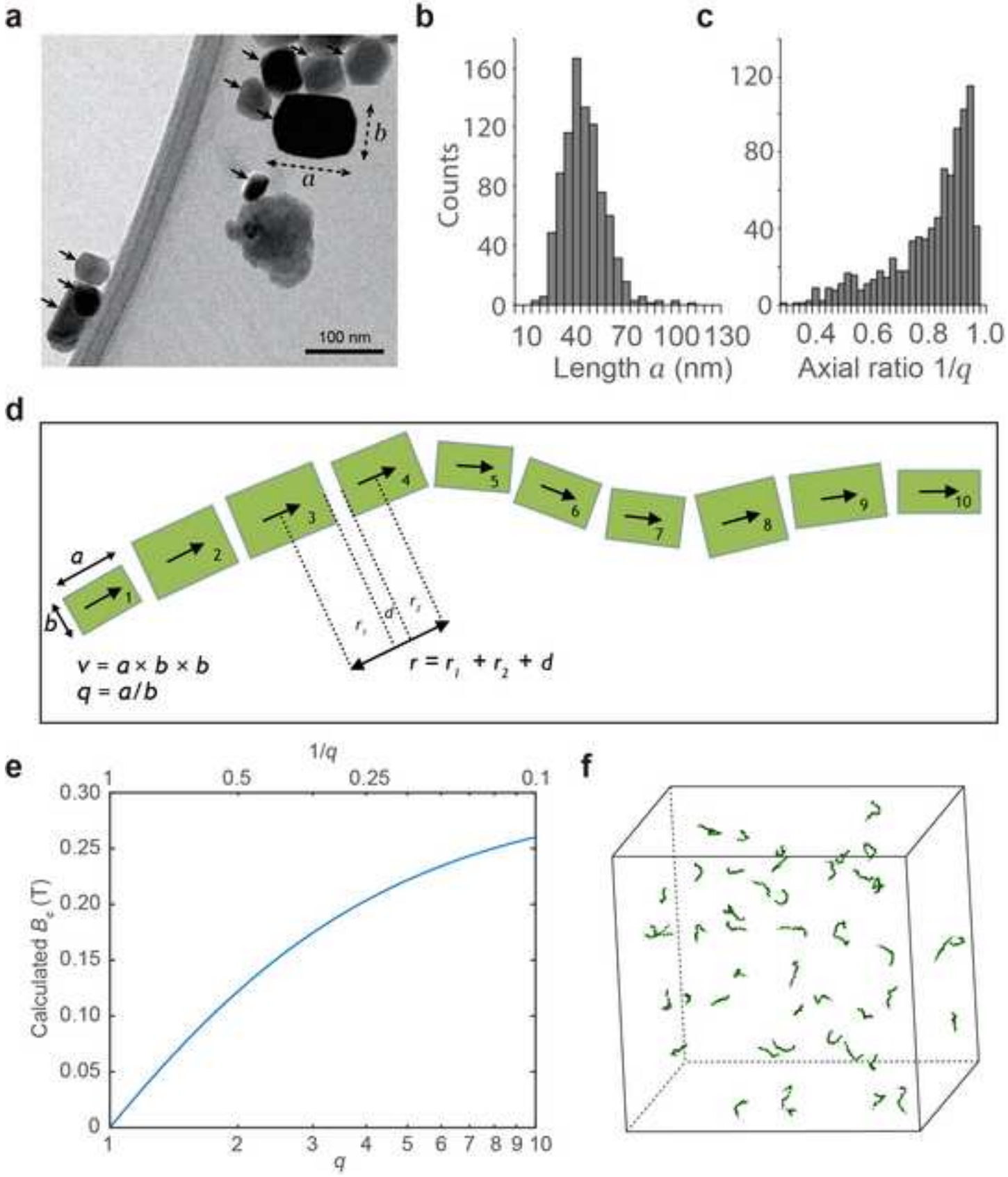

Figure 2

Click here to download high resolution image

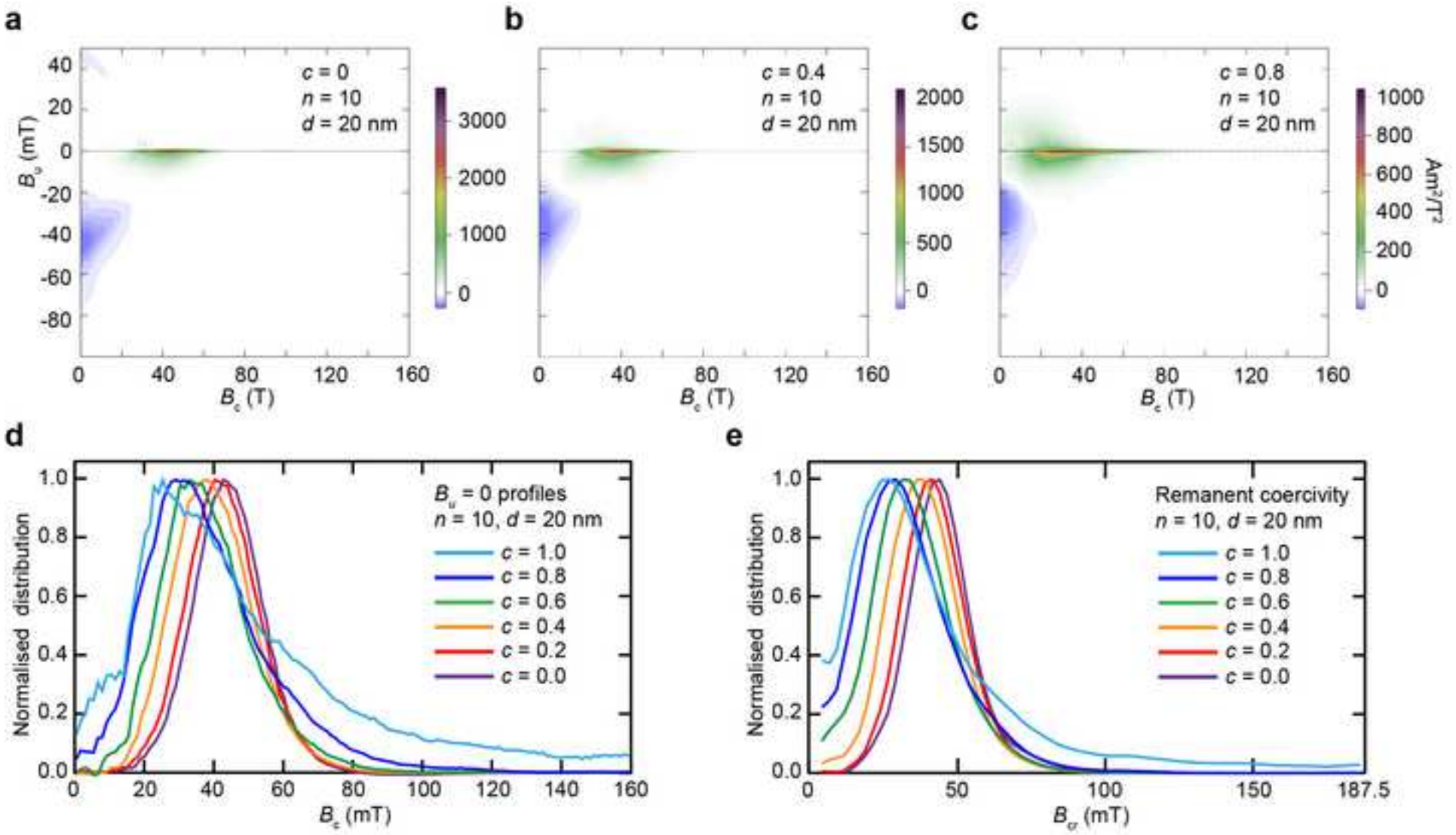

Figure 3

Click here to download high resolution image

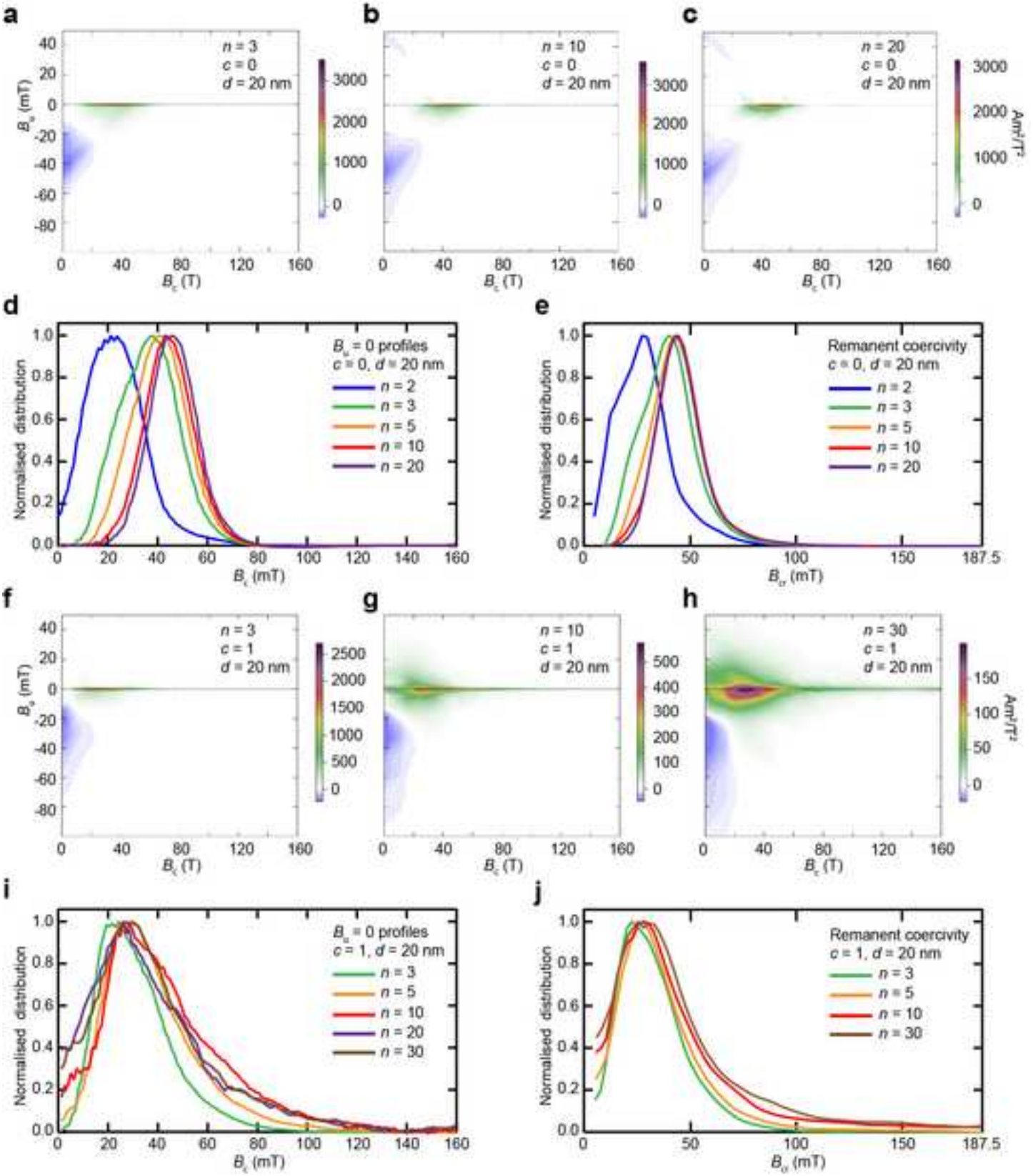

Figure 4

Click here to download high resolution image

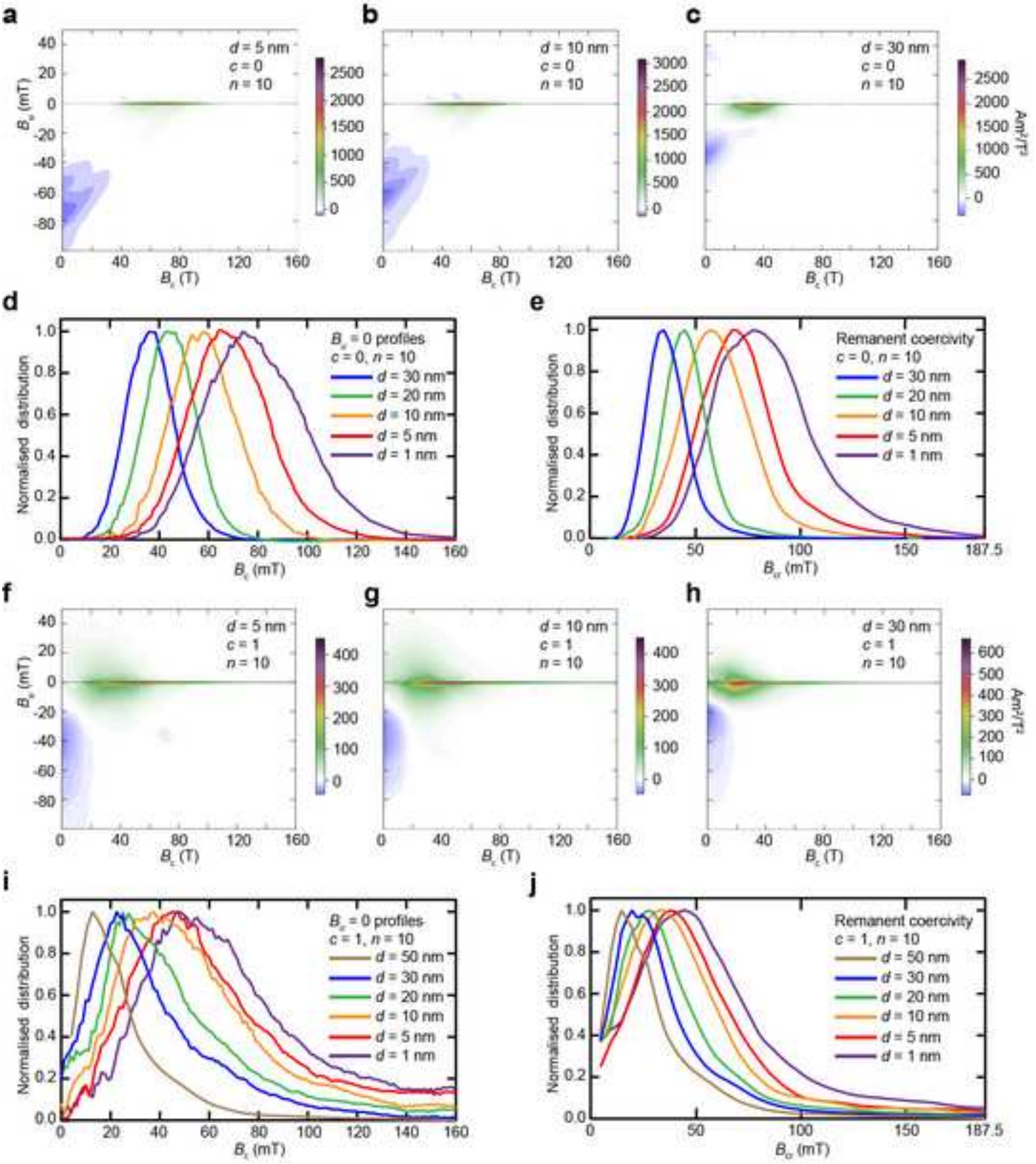

Figure 5

Click here to download high resolution image

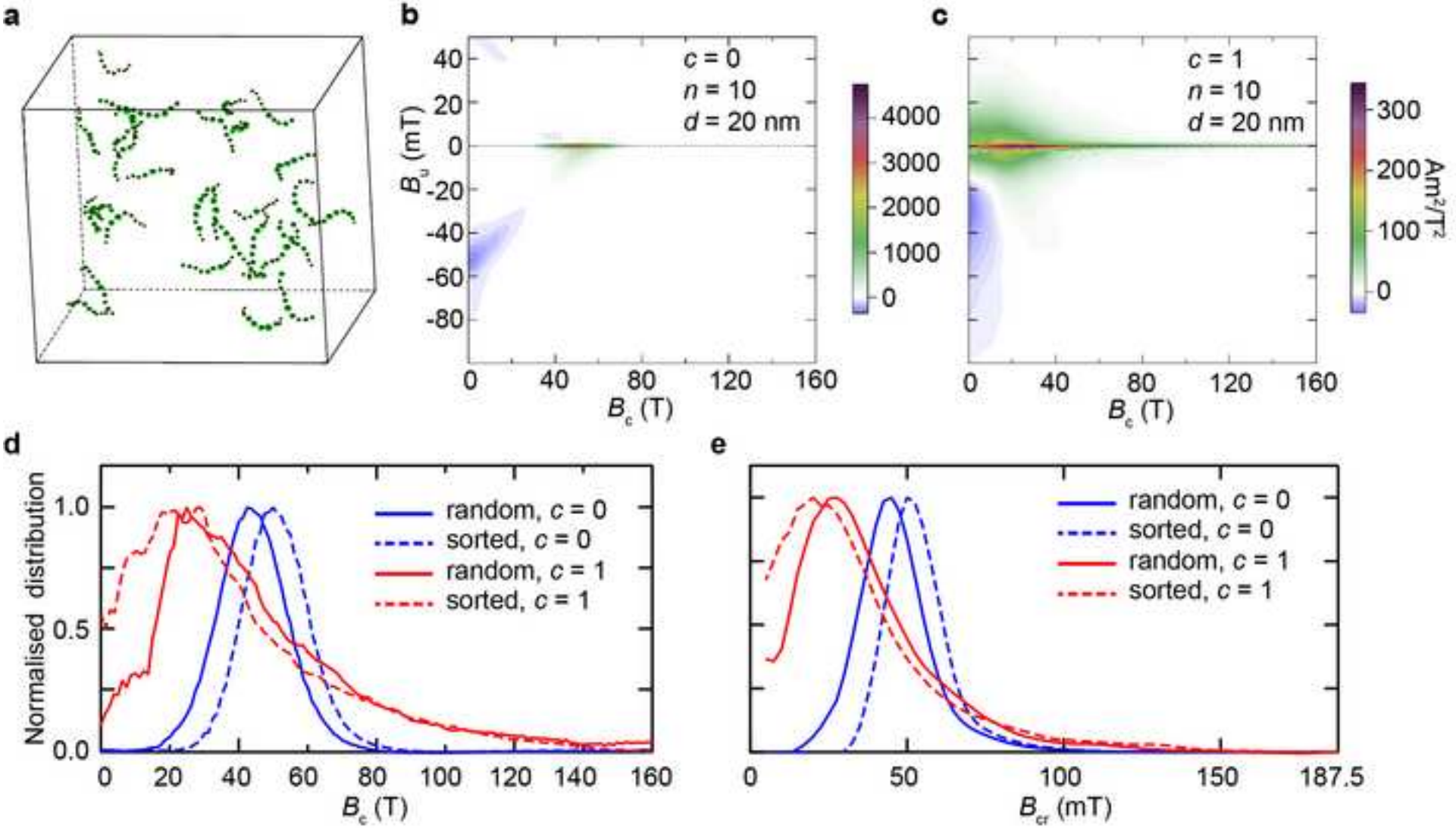

Figure 6

Click here to download Figure: Fig.6.eps

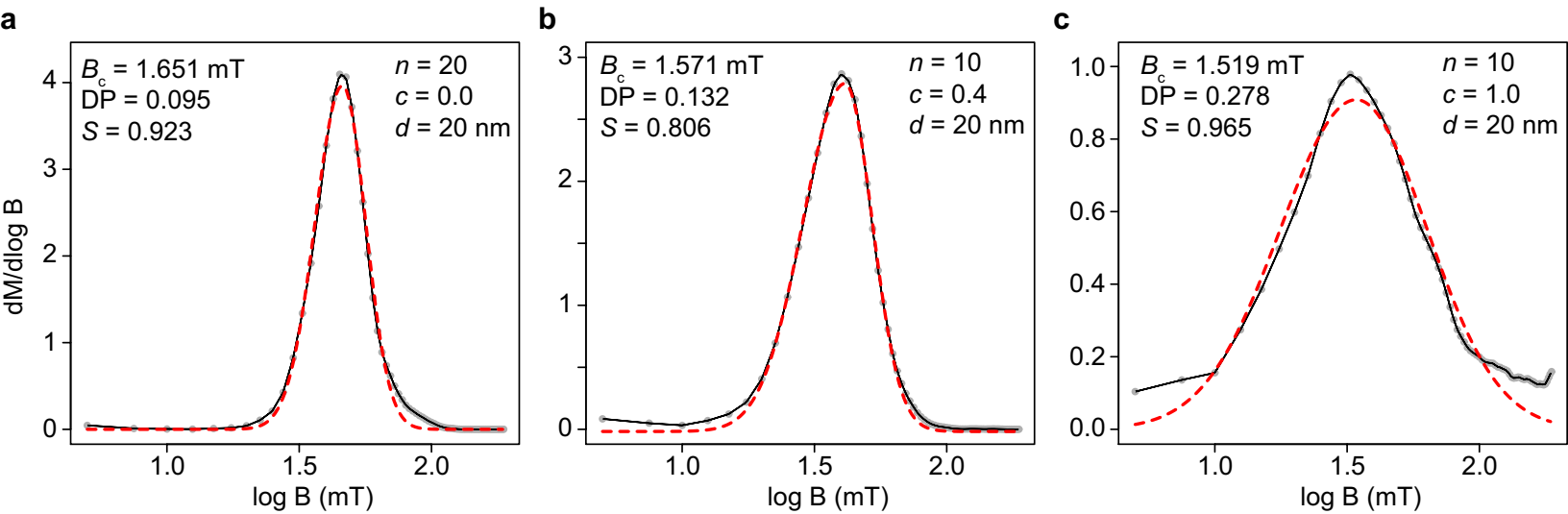

Figure 7

Click here to download Figure: Fig.7.eps

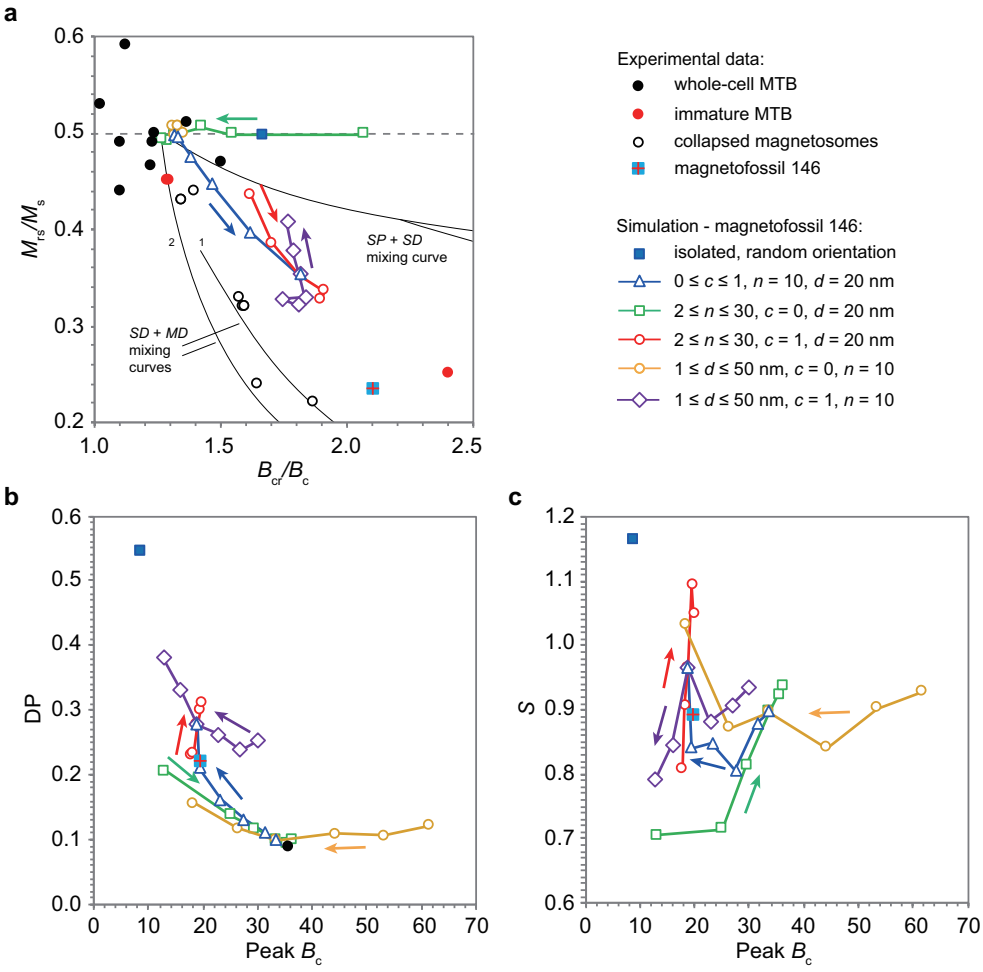

Figure 8
Click here to download Figure: Fig.8.pdf

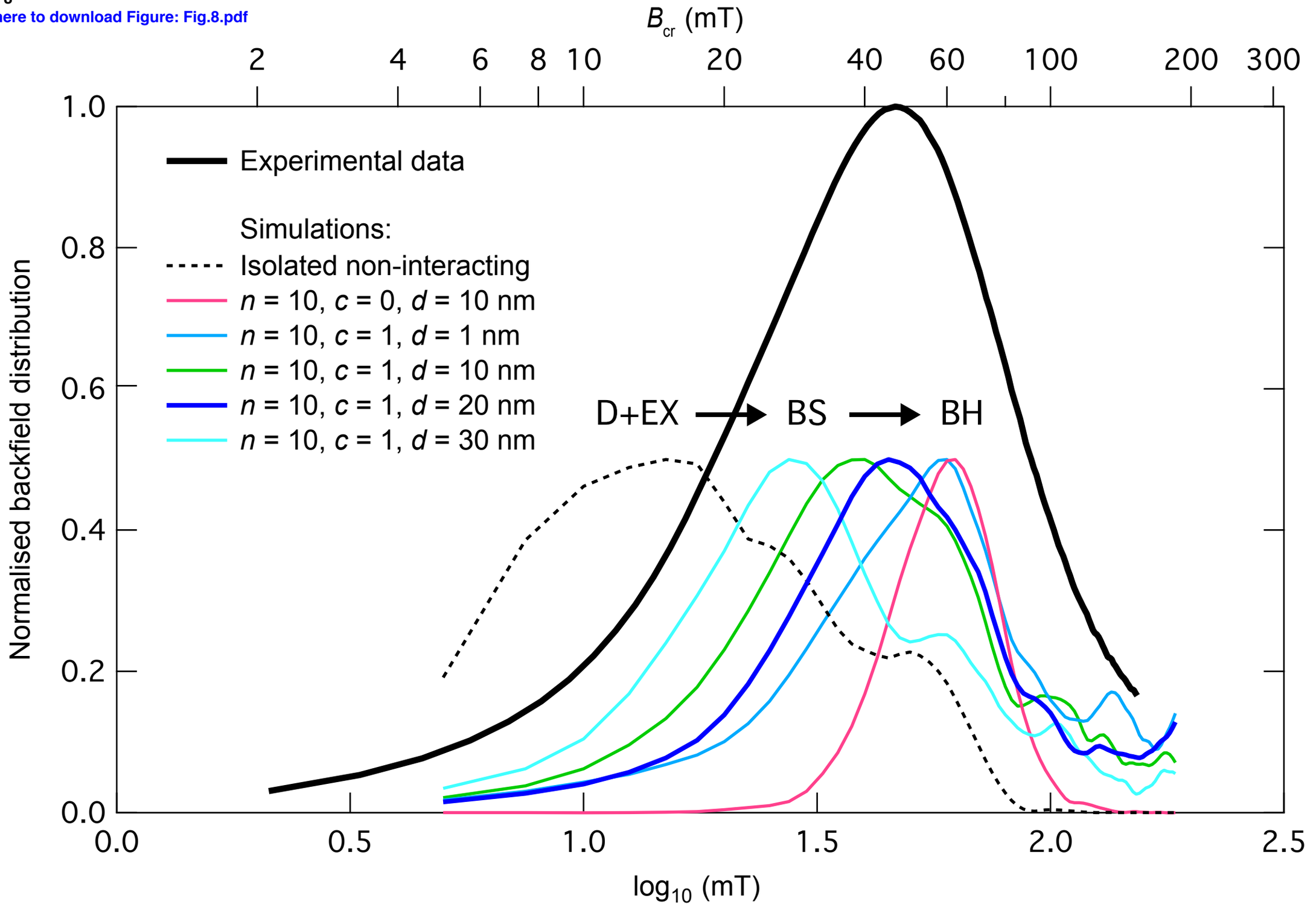

Supplementary material for online publication only

Click here to download Supplementary material for online publication only: Supplementary.docx